iScience

CellPress
OPEN ACCESS

Review

NIR-quantum dots in biomedical imaging and their future

Hélio M. Gil,[1,2] Thomas W. Price,[1] Kanik Chelani,[1] Jean-Sebastien G. Bouillard,[3] Simon D.J. Calaminus,[4] and Graeme J. Stasiuk[1,*]

SUMMARY

Fluorescence imaging has gathered interest over the recent years for its real-time response and high sensitivity. Developing probes for this modality has proven to be a challenge. Quantum dots (QDs) are colloidal nanoparticles that possess unique optical and electronic properties due to quantum confinement effects, whose excellent optical properties make them ideal for fluorescence imaging of biological systems. By selectively controlling the synthetic methodologies it is possible to obtain QDs that emit in the first (650–950 nm) and second (1000–1400 nm) near infra-red (NIR) windows, allowing for superior imaging properties. Despite the excellent optical properties and biocompatibility shown by some NIR QDs, there are still some challenges to overcome to enable there use in clinical applications. In this review, we discuss the latest advances in the application of NIR QDs in preclinical settings, together with the synthetic approaches and material developments that make NIR QDs promising for future biomedical applications.

INTRODUCTION

Current imaging techniques used in a clinical setting include magnetic resonance imaging (MRI), computed tomography (CT), positron emission tomography (PET), single-photon emission computed tomography (SPECT), and ultrasound. Each of these techniques has strengths and limitations; for example, MRI can produce high-resolution anatomical and functional images, with high tissue penetration, without using ionizing radiation, yet suffers from poor image contrast. PET offers a highly sensitive imaging modality, yet suffers from poor resolution, requires ionizing radiation, and will usually be paired with an anatomical technique such as MRI or CT (Judenhofer et al., 2008). Furthermore, most of these imaging techniques require large, expensive machines to produce these images, have scanning times on the order of minutes to hours, and have significant image reconstruction periods associated with them (Alkhybari et al., 2018; Leigh et al., 2002). Ultrasound stands out in contrast to this, allowing for real-time image acquisition and reconstruction using handheld equipment; however, it has limitations in terms of tissue penetration and image contrast.

Fluorescence imaging is an alternative modality that can offer real-time imaging with high contrast and resolution, although it has similar issues with tissue penetration (Cao et al., 2019; Huang et al., 2019; Zhang et al., 2019a). Fluorescent imaging typically involves the administration of an exogenous probe to allow for signal generation. Excitation of these agents through the application of light of an appropriate wavelength causes them to fluoresce; collection of this emitted signal produces the image. This imaging modality is of great benefit for diagnosis, with preclinical applications for tumor identification and brain injury being demonstrated (Li et al., 2020). It has also been shown to be applicable to single-cell tracking (Awasthi et al., 2020) for studying the immune system and circulating tumor cells and has also been applied to fluorescence-guided surgery (Tian et al., 2020).

When focusing on the biological applications of fluorescent probes, and imaging with these probes, there are ideal characteristics that they should possess. They must be selective for the target, possess low toxicity for the organism, and have excellent fluorescent properties (i.e. high photoluminescent quantum yield [PLQY], photostability, tuneable emission) that allow visualization of the probe's localization/distribution with a reasonable tissue penetration depth. Recent advances in fluorescent imaging have pushed the maximum reported tissue

[1]Department of Imaging Chemistry and Biology, School of Biomedical Engineering and Imaging Sciences, King's College London, 4th Floor Lambeth Wing, St Thomas' Hospital, London SE1 7EH, London, UK

[2]Department of Biomedical Sciences, Faculty of Health Sciences, University of Hull, Cottingham Road, HU6 7RX Hull, UK

[3]Department of Physics and Mathematics, University of Hull, Cottingham Road, HU6 7RX, Hull, UK

[4]Centre for Atherothrombosis and Metabolic Disease, Hull York Medical School, Faculty of Health Sciences, University of Hull, Cottingham Road, HU6 7RX, Hull, UK

*Correspondence: graeme.stasiuk@kcl.ac.uk

https://doi.org/10.1016/j.isci.2021.102189

This is an open access article under the CC BY-NC-ND license (http://creativecommons.org/licenses/by-nc-nd/4.0/).

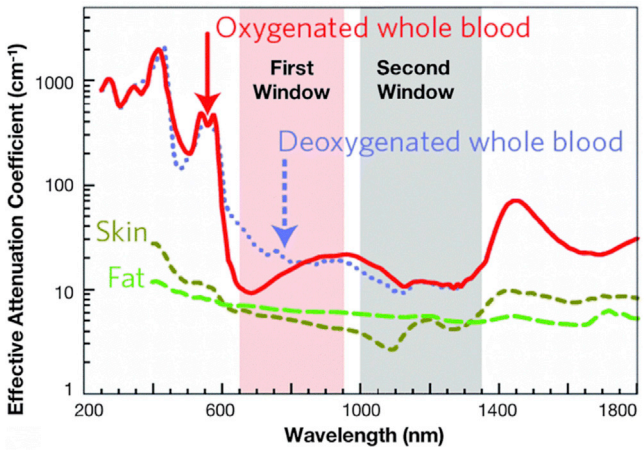

Figure 1. NIR-I and NIR-II optical transparency windows in some biological tissues and fluids

These plots of effective attenuation coefficient (on a log scale) versus wavelength show the quantitative relevance of different body substances (oxygenated blood, deoxygenated blood, skin, and fatty tissue) when aiming for deep sub-skin imaging. Adapted with permission from (Smith et al., 2009).

depth, from 3.2 cm to 8 cm, and allowed for the whole imaging of a live rat and also the tracking of 100 μm particles through the gastrointestinal tract of a live mouse (Dang et al., 2019).

Fluorescent probes can be small organic molecules (e.g. cyanine, rhodamine, or BODIPY), metal complexes (e.g. Ir, Ru, Ln), fluorescent proteins (e.g. GFP), polymers, or nanoparticles. A key part of the fluorescent probe is the organic dye. Unfortunately, many organic dyes have the significant limitation that their excitation and emission lie within the ultraviolet (UV)-visible region, outside the biological transparency windows. In biological applications the exciting or emitted light may be absorbed by water, hemoglobin, oxygenated hemoglobin, skin, fat, proteins, and cell structures (Hemmer et al., 2016; Zhao et al., 2018). This hampers the use of this technique and limits its application to regions close to the surface of the sample or patient being monitored when using light in the UV-visible range (Zhang et al., 2016). Furthermore, there is a background signal, or autofluorescence, produced by tissues within the body when excitation wavelengths within the UV-visible range are used; this reduces the contrast and image quality obtained.

The near-infrared (NIR) region of the electromagnetic spectrum is seen as ideal for fluorescence imaging. The scattering, absorption, and auto-fluorescence from tissues is greatly reduced in this region. This should allow for improved image quality and greater tissue penetration, broadening the applications of this technique for diagnosis of disease and monitoring of treatment. The NIR region can be further separated into NIR-I (between 650 and 950 nm) and NIR-II (between 1000 and 1400 nm), the so-called NIR biological windows. It is within these windows that the interference of biological media is lowest (Figure 1).

Quantum dots (QDs) are a subset of nanoparticles and given their properties, can be used as fluorescent NIR probes, as an alternative to organic dyes.

QDs are typically inorganic semiconductor nanoparticles, with the exception of carbon QDs, with sizes usually below 50 nm. The distinct optical properties observed in these compounds, when compared with their bulk counterparts, are due to the existence of quantum confinement effects. The quantum confinement effects that are observed are directly influenced by the material's composition and physical dimensions. In bulk semiconductor materials there is a band-gap energy (*Eg*) that represents the difference between the highest occupied energy state of the valence band and the lowest unoccupied state of the conduction band. When an electron in the valence band absorbs a photon with energy equal to, or higher than *Eg*, it becomes excited and transitions to the conduction band. This leaves behind an "electron hole." The negatively charged electron and the positively charged hole form a quasi-particle called an exciton. When the electron relaxes back to the valence band, it annihilates the exciton and may release energy in the form of a photon, with energy lower than *Eg* (due to energy lost in the transition), in a process called radiative recombination.

The exciton has a finite size within a crystal that is defined as the exciton Bohr radius. When the size of the semiconductor crystal is smaller than the size of the exciton Bohr radius, quantum confinement effects arise, the charge carriers become spatially confined, and the energy levels become discrete. Therefore, the exciton Bohr radius defines the transition point between the different properties observed in the bulk state and in the quantum confined state. In the latter, small variations in the size of the nanocrystals lead to size-dependent absorption and emission profiles. The control of the particle size becomes the handle by which the optical properties of the QD can be tuned (Buhro and Colvin, 2003).

As a consequence of these interesting characteristics, QDs have been extensively studied and have found applications in different areas such as optoelectronic devices, biological imaging, and solar energy devices (Jamieson et al., 2007).

QDs probes have some unique properties that make them particularly favorable for fluorescent imaging applications. These include

- Size-modulated absorbance and emission, allowing for the production of probes made of the same material with different optical properties for multiplexing purposes (Yu et al., 2019; Zhao et al., 2018).
- High photostability, allowing imaging for extended periods of time without loss of signal—potentially favorable for fluorescence-guided surgery (Jain et al., 2008; Zhao et al., 2018).
- Large Stokes shift: this simplifies filtering out the excitation light and also allows for multicolor imaging using a single excitation wavelength (Yu et al., 2019; Zhao et al., 2018).
- High brightness resulting from their large excitation cross-section, allowing for improved sensitivity, which in turn allows for imaging at the receptor concentration level (Zhao et al., 2018).
- Despite having similar PLQYs in the UV-visible range, QDs have superior PLQYs to organic dyes in the NIR range (Resch-Genger et al., 2008).
- Longer lifetime of the excited state, potentially allowing for the development of probes that can be used for time-delayed microscopy to avoid the autofluorescence of cells and other moieties (Pons et al., 2019; Resch-Genger et al., 2008).
- High-surface area-to-volume ratio that allows for efficient functionalization with other imaging agents, creating a multimodal probe, allowing imaging of disease states at different scale lengths and different tissue depths (Stasiuk et al., 2011).

NIR QDs are a specific class of fluorescent probes that emit in the NIR region of the spectra and stand as one of the most promising materials used in pre-clinical setting. Their small size (up to 30 nm), excellent PLQY (up to 45% in aqueous media), high photostability, and biocompatibility are their main advantages over the traditional molecular dyes (Resch-Genger et al., 2008). Furthermore, the possibility to load the surface of these QDs with specific targeting motifs and therapeutic agents creates the possibility to engineer a whole new class of theranostics with enhanced properties (Li et al., 2019c; Liu et al., 2020a; Zhao et al., 2020). Thus, further development of QDs as NIR probes for biomedical imaging could be the key to future success of this imaging modality.

In this review we discuss the different methodologies through which QDs are synthesized and the different classes of materials that compose these QDs, with a focus on NIR QDs. After establishing the materials used in these nanoparticles, we discuss the state-of-the-art in biomedical fluorescence imaging, highlighting the possibility for image-guided surgery with NIR QDs. In a final remark, we highlight the future perspectives and challenges that the field still has to overcome to see the NIR QDs implemented in a clinical setting.

SYNTHESIS OF NIR QDS

Since the discovery of an efficient method to synthesize QDs in 1993, Cd(II) and Pb(II) have been used as the base metal for the fluorescent core of the nanoparticles (Murray et al., 1993). Although the QDs obtained show excellent properties and NIR emission, toxicity problems due to the leaching of heavy metals have been a major drawback for their application in biological systems (Allocca et al., 2019; Brunetti et al., 2013).

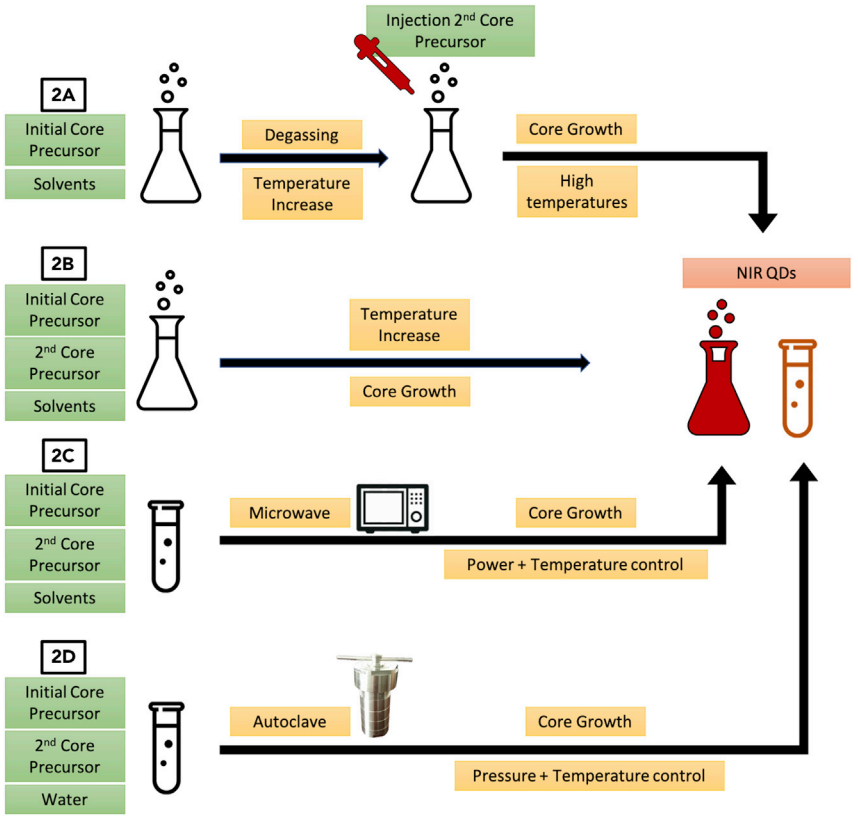

Figure 2. Overview of the synthetic methodologies used for NIR QDs

(A–D) (2A) Hot-injection: in the first step, one initial precursor is mixed with the reaction solvent and degassed under vacuum and argon. Then, the temperature is elevated close to the nucleation temperature and the second core precursor is injected. The core growth is performed at high temperature and the NIR QDs are synthesized; (2B) Heat-up: all of the core precursors and reaction solvents are mixed at room temperature, and the temperature is gradually increased up to the nucleation threshold. Core growth takes place and NIR QDs are synthesized; (2C) Microwave: similar to the heat-up method, QD precursors and reaction solvents are mixed in a microwave vessel. The vessel is then placed in a microwave and submitted to controlled power and temperature output for a short period of time. (2D) Hydrothermal: precursors are mixed in water at room temperature and then added to a Teflon-lined autoclave. The system is closed and submitted to high temperature and pressure, allowing the formation of water-soluble NIR QDs.

In recent years, the synthesis of NIR QDs has evolved toward the integration of new materials such as Ag(I), Cu(I), and more recently carbon dots (Li and Wu, 2019a; Li et al., 2019c; Zhang et al., 2020). These present safer alternatives to the classical QDs, while even improving upon some of the photophysical properties. The synthetic methodologies that have been developed up to the present day focus on surface modifications as means to improve the biological compatibility and at the same time increase the fluorescent properties by shifting the emission toward longer wavelengths.

Synthetic methodologies

The main synthetic methods used in the synthesis of NIR QDs are hot-injection, heat-up, microwave, and hydrothermal synthesis (Figure 2). They possess different advantages and are used in different circumstances depending on the nature of reagents, solvents, and the desired coating of the final product. In-depth reviews on these synthetic methodologies have been conducted (Reiss et al., 2016; Tamang et al., 2016; van Embden et al., 2015), and in this section we present a summary, for a better understanding of the following sections.

The hot-injection method (Figure 2A) was first introduced by the works of Murray and co-workers (Murray et al., 1993), and it remains the most common method used to synthesize a wide variety of monodisperse QDs. Despite the benefits and the control that a hot-injection synthesis offers for the production of QDs,

this method still suffers from some drawbacks. The high temperature of the reaction results in rapid reaction rates; as such, mixing of the reagents must be efficient to produce monodisperse nanoparticles. This is more difficult to achieve as the reaction volume increases; when the volume crosses a threshold limit the homogeneity of the batch is less reproducible, making this method less suitable for large-scale QD production than other methods.

The heat-up synthetic method (Figure 2B) for QDs is a single-pot reaction without an injection step. The nucleation period in this technique is usually spread over a long period of time, and because of this some precursors start to nucleate at different time points (van Embden et al., 2015). This leads to an increased polydispersity in size distribution. Another major drawback of this technique is the need to employ reagents that have similar reactivities at the desired reaction temperatures (Chen et al., 2016). Matching the reactivity of the ligands and precursors ensures that the nucleation occurs in a short window and generates enough nuclei. The search for a larger library of reagents and solvents is thus one of the priorities for the advancement of this technique.

The microwave method (Figure 2C) makes use of electromagnetic radiation to achieve a rapid and homogeneous heating of the reaction. The control over the rate of heating during the synthesis offers the potential for better control over the formation of the QDs (Sinatra et al., 2017), which have been exploited to improve monodispersity in a reproducible manner. These intriguing properties make this method a viable alternative to hot-injection methodology with respect to the monodispersity of the QDs. Nonetheless, this method is still in its early stages of development and the QDs obtained usually have low PLQY, hindering their applications. The requirement for a polarizable solvent makes the direct comparison to other methods difficult, as the aliphatic solvents used are not suitable for microwave-based synthetic procedures (Sun et al., 2016).

The hydrothermal method (Figure 2D) refers to the use of aqueous solvents at high temperature and pressure for the synthesis of QDs (Sonawane et al., 2018). The synergetic effect of these conditions leads to the rapid formation of nuclei, resulting in monodisperse QDs that do not require post-synthesis treatments in order to be compatible with aqueous media. The hydrothermal method is often preferred when the final application of the synthesized QDs is biological. It is the most employed variation of aqueous synthesis of QDs, although the drawback of this method is the weak photophysical properties of the QDs obtained. Post-treatment with methods such as size-selective precipitation, photochemical etching, and surface modifications are usually employed in order to improve their properties (Wei et al., 2018).

All of the techniques above represent a different method of obtaining QDs, with advantages and disadvantages. Hot-injection and heat-up methods are the most used and consist of using high temperatures in order to control the nucleation and growth of QDs, but the reaction conditions are difficult to precisely control and reproducibility is hard to achieve. Hydrothermal and microwave are faster and enable a better control of the reaction conditions, but further optimizations are still required to achieve better optical properties of the synthesized QDs.

QDS materials

The methodologies described in the previous section have been used to synthesize QDs with different materials in their structure. In the next section, we discuss the most used materials in the synthesis of NIR QDs and the properties obtained using different synthetic methodologies.

Cadmium-based NIR QDS

Cd(II)-based QDs have been the most studied and applied material for QDs. The synthesis of Cd(II)-based QDs is one of the easiest from a synthetic point of view. The core precursors, which can vary from CdO (Peng and Peng, 2001) to $CdCl_2$ (Cui et al., 2018), are injected into a hot solution of the solvents and stirred for 30 to 60 min to yield NIR-emitting QDs (Figure 3). The solvent used in the synthesis has changed over the years from predominantly phosphine-based ones (tetradecylphosphonic acid, octadecylphosphonic acid) to fatty acids (oleic acid, 1-octadece) (Peng and Peng, 2001). This change was driven by a necessity to adhere to a more environmentally friendly chemistry, and at the same time, fatty acids also allow for an easier transition between crystal shapes. This change in shape allows for the appearance of higher energy transitions in the crystal structure of the QDs, thus extending the emission toward longer wavelengths. Cd(II)-based NIR QDs that have been published in recent years comprise CdS (d = 3.7 nm, λ_{ex} = 468 nm,

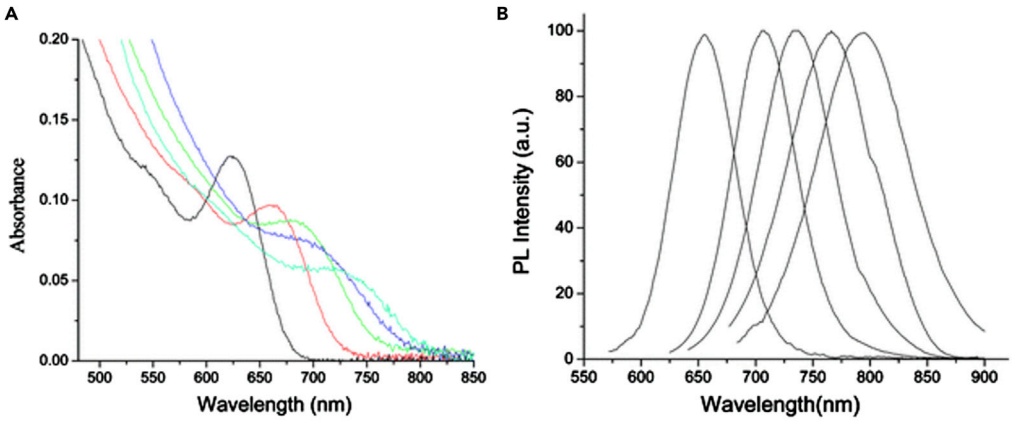

Figure 3. Overview of NIR Cd-based (CdTe/CdS) QDs' optical features, synthesized via hydrothermal method

(A and B) (A) UV-visible absorption and (B) corrected PL spectra of NIR-emitting NAC-capped CdTe/CdS QDs prepared from various reaction times (λ_{ex} 400 nm). The emission peak of these QDs occurs in the first window of the NIR range, up to 895 nm after 69 min of reaction time. Adapted with permission from (Zhao et al., 2009). Copyright © 2009, American Chemical Society.

λ_{em} = 730 nm), CdTe (d = 5.7 nm, λ_{ex} = 576 nm, λ_{em} = 606 nm), and some alloyed compounds as well (Cui et al., 2018; Saikia et al., 2017).

The synthetic methodologies for Cd(II)-based QDs can yield organic-phase QDs and also water-soluble QDs that are biologically compatible. One route to the synthesis of water-soluble CdS NIR QDs (d = 3.7 nm, λ_{ex} = 468 nm, λ_{em} = 730 nm) has been described by Cui and co-workers (Cui et al., 2018) using $CdCl_2$ in a solution of BSA. Addition of L-cysteine provides the sulfur source and reacting at 80°C for 30 min yields CdS QDs that are water soluble due to the BSA matrix. These QDs had a first excitonic peak at ~450 nm, allowing the authors to excite the QDs with an emission source at 468 nm, obtaining an emission in the first NIR region, centered at 730 nm. The resulting high-water solubility of these materials allows for the direct application of these QDs to cell imaging.

In order to optimize the optical properties of established QDs, doping of their matrix with chosen atoms is becoming a fast-growing research field. This can produce a blue or red shift in the emission maximum, alter the absorbance profile, or increase the PLQY of the QDs. These changes are achieved by modifying the semiconductor properties of the material, including the energy band-gap value. CdSe compounds usually have emissions in the visible range but doping of certain atoms, such as silver, gives rise to more sub-band-gap states in the crystalline structure (Zhao et al., 2019). This phenomenon ultimately introduces more absorption peaks and extends the absorption edges of CdSe QDs into the infrared regime.

A recent study shows the production of ternary $CdS_{1-x}Ag_x$ QDs (d = 15 nm, λ_{em} = 700–800 nm, *PLQY* = 36%), in a biosynthetic method using *Escherichia coli* bacteria (Órdenes-Aenishanslins et al., 2020). This method takes advantage of the *E. coli* enzymatic activity, producing H_2S in the presence of cysteine. This volatile compound is then secreted to the surrounding area and reacts with Cd(II) ions to form CdS QDs. In addition, by the addition of different concentrations of $AgNO_3$, the Ag ions replace some of the Cd to form ternary $CdS_{1-x}Ag_x$ QDs that emit in the NIR-I window with reported PLQY of 36%. This simple and environmentally friendly method opens the possibility to use cells to produce QDs. Other studies for the biosynthesis of Cd-based QDs in different bacterial cells have been reported (Gallardo Benavente et al., 2019; Lin et al., 2020; Sur et al., 2019).

Other groups have reported ternary Cd-based QDs with different compositions. The synthesis of CdHgTe ternary QDs capped with mercaptopropionic acid (MPA) (d = 2.5–4.2 nm, λ_{em} = 730 nm) was achieved using the hydrothermal method with $CdCl_2$, $HgCl_2$, Na_2TeO_3, and MPA (Jagtap et al., 2016). By tuning the reaction time over 2–30 min, the resulting QDs size can be controlled, ranging from 2.5 to 4.2 nm and a corresponding emission in the NIR region, ranging from 650–855 nm.

Cd(II) was one of the first elements to be used in the synthesis of QDs, and the synthetic methodologies evolved around Cd(II) in order to obtain QDs with improved optical properties. In the present day, there

are reports of Cd-based QDs synthesized with different precursors, through variations of different methodologies, emitting in the NIR-I range. The best QDs are obtained via the hot-injection and heat-up methods, with PLQY approaching near unity in organic solvents and with sub-10 nm sizes (Elibol, 2020). After surface functionalization or through hydrothermal synthesis, Cd(II) QDs can be dispersed in aqueous media and be suitable for biological applications. Nonetheless, despite the large amount of research with this material for its use in biomedical applications, the toxicity associated with this heavy metal is a major concern.

Copper-based NIR QDS

The use of Cu(I) as a metal for the cores of NIR QDs has increased in the past years, both as a dopant and as a component of ternary QDs. The incorporation of copper in this manner results in a broadened emission profile, alongside a bathochromic shift in the emission maxima.

The most represented examples of QDs that incorporate Cu(I) into the core are Cu:InP and $CuInS_2$ QDs. Although InP QDs usually have an emission range in the visible region (d = 2–10 nm, λ_{em} = 450–625 nm), Cu:InP QDs have a greatly extended emission range, while maintaining the size of the particles (d = 2–10 nm, λ_{em} = 580–1110 nm) (Clarke et al., 2019; Li and Wu, 2019a; Reiss et al., 2016). This doping has other beneficial effects on the optical properties of these QDs: a larger Stokes shift, longer emission lifetimes, emission maxima in the NIR range, and improved chemical stability (Pradhan et al., 2017).

Recently, Kays and co-workers studied the influence of ZnS shelling (d = 4.5–10 nm, λ_{em} = 682 nm) and Zn doping of $CuInS_2$ QDs (d = 3.5 nm, λ_{em} = 822 nm) on their toxicity. The synthesis followed a hot-injection method, by adding the sulfur precursor hexamethyldisilathiane into a solution of Cu(II) and In(III) salts with TOP and ODE as solvents (Kays et al., 2020). Shelling the bare $CuInS_2$ cores with ZnS reduced the wavelength of the emission maxima from 822 to 681 nm, whereas the diameter increased from 3.5 to 4.5 nm. Zinc doping showed just a slight blue shift in the emission maxima from 822 to 808 nm with no change in diameter. The results showed a reduction of toxicity in mice and in the human liver cancer cell line HepG2. Using a moderate *in vivo* dose of 15 mg kg^{-1}, the non-shelled particles induce severe hepatotoxicity and splenotoxicity, whereas *in vitro* tests demonstrate cell viability <20% with doses greater than 0.2 mg mL^{-1}. In contrast, the ZnS-shelled $CuInS_2$ QDs do not reduce the cell viability at this concentration. This demonstrates the fact that although $CuInS_2$ QDs can be considered for NIR imaging, appropriate shelling methods must be developed in order to avoid the leaching of ions from the core.

Xia and co-workers have also synthesized $CuInS_2$/ZnS QDs (d = 3–8 nm λ_{em} = 750–1100 nm) that can emit in the NIR windows (Xia et al., 2017). The synthetic approach aimed at obtaining wurtzite $CuInS_2$ structures, contrary to the chalcopyrite that are usually obtained through direct methods. The authors hypothesized that this hexagonal wurtzite structure would allow $CuInS_2$ QDs to emit at higher wavelengths. The authors first synthesized CuS structures using a hot-injection method and then performed a cation-exchange, replacing Cu(I) ions with In(III), by slowly adding $In(Ac)_3$ precursor. Following shelling, the resulting $CuInS_2$/ZnS QDs showed emission peaks at longer wavelengths, from 750–1100 nm depending on the size of the crystal (3–8 nm). $CuInS_2$/ZnS QDs synthesized in this way (d = 4.7 $\pm$ 0.5, λ_{em} = 820 nm) had a PLQY of 75% in chloroform.

Kubicek-Sutherland and co-workers also described the synthesis of alloyed Cu(I)-based NIR QDs (Kubicek-Sutherland et al., 2020). The CuInSeS/ZnS QDs (d = 7–10 nm, λ_{em} = 550–1200 nm, *PLQY* > 95%) were synthesized by optimizing a previously described hot-injection method, producing sub-10 nm QDs with promising fluorescent properties in the NIR-I biological window, by changing the Se/S ratio. The cytotoxicity of the QDs was also tested on mouse fibroblast cells and shown to be less toxic than commercially available CdSe/ZnS and InP/ZnS QDs. The difference in toxicity was visible after 6 days of incubation of 100 μg mL^{-1} QDs with the mouse fibroblast L929 (CCL-1) cell line. Although both the Cd(II) and In(III) QDs reduced the viability of the cells to below 50%, the Cu(I) QDs had almost no effect on the viability of the studied cells. The tissue penetration was also evaluated, with the QDs fluorescence being detected through 32 mm of a hemoglobin solution and through 3.5 mm of turkey meat (tissue phantom). These results highlight once more the favorable optical and biological properties of Cu(I) QDs for biomedical applications.

These results show that incorporating Cu(I) into QDs with an In-based core can greatly alter their optical properties, making them suitable for NIR imaging without compromising on the already established size and PLQY. Nonetheless, the incorporation of Cu(I) does not solve the toxicity issues that many QDs

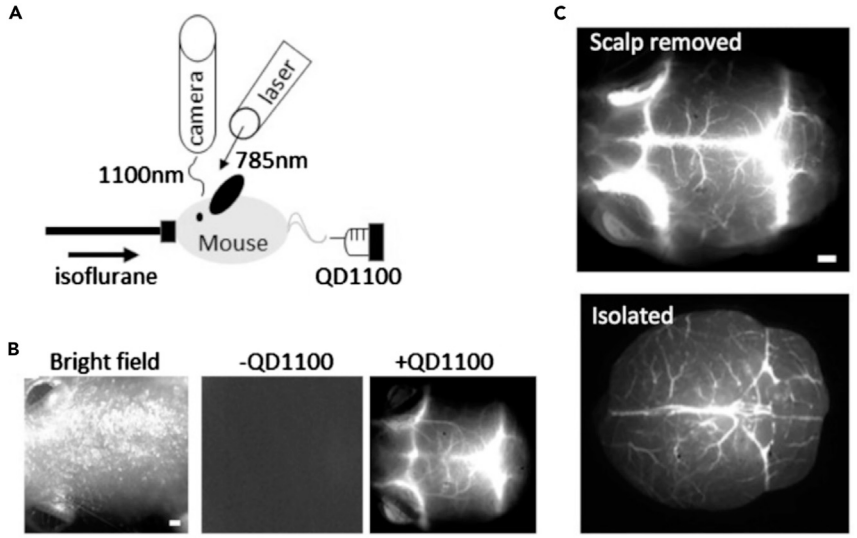

Figure 4. NIR-fluorescence imaging of mouse brain before and after treatment with PbS QDs

(A–C) (A) Experimental setup for NIR fluorescence imaging of cerebral blood vessels. An anesthetized mouse was administered QD1100 (PbS QDs) in a caudal vein. An optical laser (785 nm wavelength) was used as an excitation light source, and NIR fluorescence was detected with an InGaAs camera. (B) Imaging of a mouse head. Bright field image (left), NIR fluorescence image without QD administration (middle), and the NIR fluorescence image with QD administration (right). Scale bar: 1 mm. (C) NIR fluorescence images of cerebral blood vessels. Upper: fluorescence image after scalp removed; lower: fluorescence image after isolation. Scale bars: 1 mm. Adapted with permission from (Imamura et al., 2016).

show, and careful control of the surface chemistry is required before these QDs can be safely used in biological applications.

Lead-based NIR QDS

The first report of the colloidal synthesis of Pb-based NIR QDs was published by Murray and co-workers in 2001 (Murray et al., 2001). This work described the synthesis of PbSe QDs (d = 3–9 nm, λ_{em} = 1200–2200 nm), using the hot-injection method of TOP-Se and Pb(II) oleate precursors into a solvent solution at 150°C. This resulted in a series of QDs with sizes ranging from 3.5 to 15 nm by tuning the reaction temperature from 90°C to 220°C. This wide range of sizes is reflected in the optical properties of the QDs, with the smallest QDs presenting an exciton absorption at 1200 nm and the largest particles at 2200 nm, therefore positioning all of them in the second NIR window.

Given their excellent emission profile in the NIR window, Pb-based QDs have been synthesized with the goal of developing functional probes for *in vivo* imaging. NIR-emitting PbS QDs (d = 3–9 nm, λ_{em} = 1100 nm, PLQY = 8%) have been used for *in vivo* fluorescence imaging of cerebral blood vessels in mouse (Imamura et al., 2016). The synthesis followed a hot-injection methodology, where the reaction of $PbCl_2$ and hexadimethyldisilathiane in a mixture of oleylamine and oleic acid resulted in the formation of PbS QDs coated with oleylamine. The surface was modified with mercaptoundecanoic acid after synthesis, to grant dispersibility in aqueous phase. These PbS QDs present an emission peak at 1100 nm with a relatively low PLQY of 8% in water. Despite this, the use of these QDs allowed for the non-invasive imaging of septic encephalopathy in mice (Figure 4), and it highlights the usefulness of these nanomaterials in imaging of different vascular systems.

Although their tuneable emission across the NIR range makes PbS QDs very promising, they are prone to surface oxidation and suffer from a significant reduction in PLQY upon phase transfer into water (Welsher et al., 2009). Coating the PbS core in a shell made up of another material is one route to prevent this, allowing this exciting material to be used for biomedical applications. Zhang et al. demonstrated a CdS shelling technique; following synthesis of the PbS cores in oleylamine at high temperatures (120°C–160°C), a CdS shell was introduced *via* cation exchange using CdO, oleic acid, and octadecene at 100°C to yield a shell with thickness 1.5 nm. Following this shelling process, the QDs were coated in PEG-amine chains to allow

for their dispersion in water. The overall diameter of the QDs was slightly increased by this process (increasing from 5.4 nm to 6.9 nm), although less than would be expected for such a shell thickness. This shelling process was accompanied by a slight blue shift in the emission maxima (1725 nm–1650 nm), which was attributed to the cation exchange reducing the size of the PbS core. An increase in PLQY (from 0.33%–3.3% to 2.2%–22%) in water was also observed. The shelling procedure was also demonstrated to improve the photostability under laser irradiation over 2 h and the stability of the QD emission when incubated in PBS over 28 days. In addition to passivating the core surface, the difference in bandgap between the CdS shell and PbS core ensures that the electrons and holes are localized in the PbS core, thus resulting in a core-shell QD that retains the optical properties of the PbS core (Kim et al., 2015).

In a similar way to Cd(II), Pb(II)-based QDs use the hot-injection and heat-up methods in order to synthesize materials that would emit in the NIR range. One of the advantages of using Pb(II) as the core element is the emission in the second window of the NIR (1000–1400 nm), whereas Cd(II) materials generally emit in the first window (700–950 nm). This would benefit imaging experiments, as the tissue autofluorescence and water absorption is minimized. In terms of PLQY, Pb(II)-based QDs have a tendency to show lower values (up to 20%) when compared with Cd(II)-based QDs (up to 45%), using the same hot-injection method, which balances the higher emission wavelength verified before. Despite these promising optical properties and several years of research invested in developing these Pb(II) and Cd(II) NIR QDs, the toxic nature of the precursors greatly hinders their clinical translation and asks for safer, biocompatible alternatives.

Silver-based NIR QDS

As seen by the previously described QDs materials, Cd and Pb QDs possess excellent optical properties, but the heavy-metal composition limits their application in imaging biological systems. Over the past few years, the interest surrounding silver chalcogenide (Ag_2X, X = S, Se, Te) QDs has grown due in part to their NIR emission, low toxicity, simple synthesis, and good core stability.

Ag_2S QDs were first synthesized in 2004 (Liu et al., 2004), with a size distribution of 5.9 $\pm$ 1.65 nm and an absorption maxima at 330 nm, without mentioning their fluorescent properties. In 2010, Wang and co-workers were the first to address the NIR emission of Ag_2S QDs through their synthesis from a single source precursor using the heat-up method previously described (Du et al., 2010). The silver precursor used was $((C_2H_5)_2NCS_2)Ag$, with additional oleic acid and oleylamine ligands in octadecene at 200°C. The as-obtained Ag_2S QDs with a size of 10.2 $\pm$ 0.4 nm exhibited NIR emission centered at 1058 nm, with a narrow full width at half maxima (FWHM) value of 21 nm. This single-source precursor synthesis was adopted by other researchers to synthesize PEG-Ag_2S QDs ($d_{hydrodynamic}$ = 26.8 nm, λ_{ex} = 808 nm, λ_{em} = 1100 nm, *PLQY* = 15.5%) (Hong et al., 2012; Zhang et al., 2014).

In 2012, Zhang and co-workers also addressed the properties of Ag_2S QDs and their cytotoxic effects on cells (Zhang et al., 2012). The synthesized Ag_2S QDs (d = 5-10 nm, λ_{em} = 1000–1320 nm, PLQY = 15.5%) were coated with PEG-DHLA and tested in breast cancer cell line (MDA-MB-468) and human glioblastoma cell line (U87 MG) for targeting experiments and in mouse fibroblast cell line (L929) for cytotoxic experiments. For the targeting experiment, the QDs were functionalized with proteins recognized by the epidermal growth factor receptor (EGFR), which has a higher level of expression in MDA-MB-468 cells than in U87 MG cells. The results showed a good targeting ability toward the MDA-MB-468 cells, exhibiting high NIR emission intensities, unlike in the U87 MG cells. This demonstrates the specificity of the QDs and the response in terms of NIR emission. In the cytotoxicity studies, Ag_2S QDs demonstrated negligible toxicity in terms of cell proliferation, apoptosis and necrosis, reactive oxygen species' production, and DNA damage in L929 cells. This comprehensive study shows the potential of Ag(I)-based QDs for biomedical imaging and provides a strong biological argument for its future development and optimization.

Ag_2Te QDs have the same excellent properties and biocompatibility as Ag_2S and Ag_2Se QDs and additionally have a narrower direct bandgap of 0.06 eV (compared to 0.93 and 0.15 of Ag_2S and Ag_2Se, respectively) (Kershaw et al., 2013). This narrow bandgap will shift the optical properties to lower energies, increasing their optical efficiency and extending the emission toward longer wavelengths (Butson et al., 2019).

Zhang and co-workers demonstrated the hot-injection synthesis of Ag_2Te QDs (Zhang et al., 2020); starting from a mixture of Ag(OAc) and 1-dodecanethiol at 120°C, injection of tributylphosphine-Te rapidly yielded Ag_2Te QDs within minutes. These were subsequently coated with an Ag_2S shell by addition of further

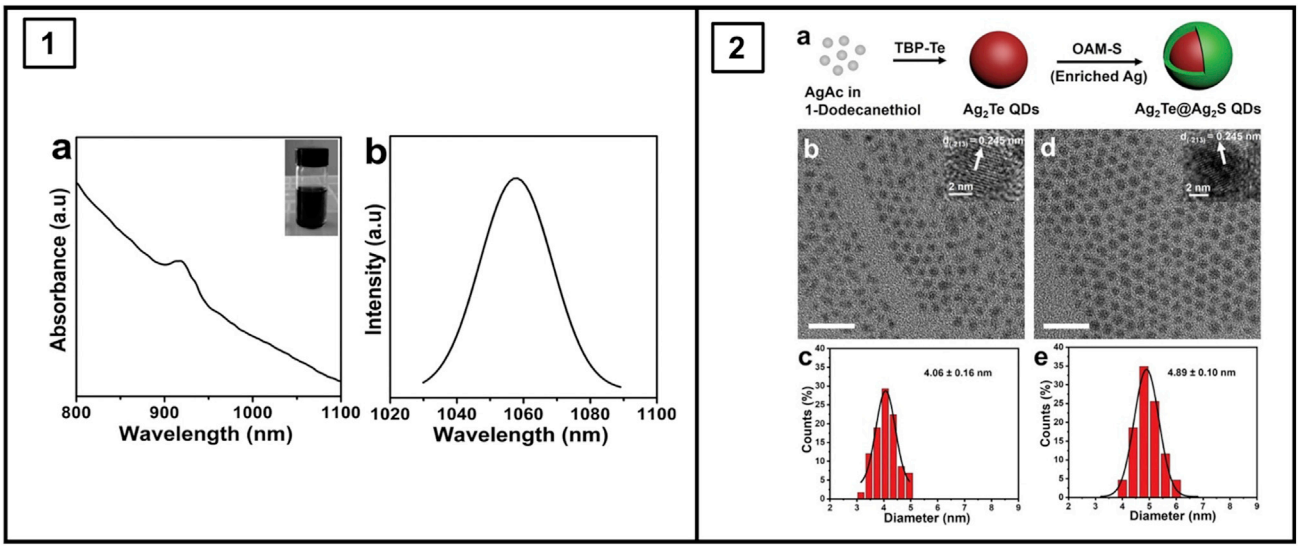

Figure 5. Optical and physical profiles of Ag-based NIR QDs

Panel 1: (A) NIR absorption spectrum of as-obtained Ag_2S QDs; the inset is a photograph of Ag_2S dispersed in cyclohexane. (B) NIR fluorescence emission spectrum of Ag_2S QDs at room temperature under λ_{ex} = 785 nm. Adapted with permission from (Du et al., 2010). Copyright © 2010, American Chemical Society.

Panel 2: Synthetic procedure of Ag_2Te@Ag_2S core–shell QDs. TEM images of (B) Ag_2Te and (D) Ag_2Te@Ag_2S QDs. Size distributions of (C) Ag_2Te and (E) Ag_2Te@Ag_2S QDs. Scale bar: 20 nm. Adapted with permission from (Zhang et al., 2020). Copyright © 2020, John Wiley and Sons.

Ag(OAc) and oleylamine-S (Figure 5, Panel 2a). The shelling process increased the diameter of the QDs from 4.06 ± 0.16 nm to 4.89 ± 0.10 nm (Figure 5, Panel 2c,e). Although both the Ag_2Te and Ag_2Te/Ag_2S QDs had emission maxima at 1300 nm, the Ag_2Te/Ag_2S QDs had a 3.2-fold greater photoluminescence intensity, with a PLQY of 4.3%. The addition of additional Ag precursors, which are readily adsorbed in the Ag_2Te surface, in the core growth stage causes an increase in the size of the core ($d(Ag_2Te)$ = 4.90 ± 1.06 nm, $d(Ag_2Te/Ag_2S)$ = 5.71 ± 0.11 nm) and a corresponding redshift in the fluorescent emission maxima from 1300 nm to 1524 nm (1560 nm upon shelling with Ag_2S). This is within the NIR-IIb region (1500–1700 nm), which is exciting for its reduced absorbance and potential for high spatial resolution *in vivo* imaging.

When analyzing the properties of Ag-based QDs, they are very on par with other well-developed materials such as Cd(II) or Pb(II). The increased size dispersion (from 5–30 nm) is more noticeable in Ag-based QDs, given the more generalized use of hydrothermal methods for their synthesis. Nonetheless, the emission range is comparable to the Pb(I) QDs, with well-reported values in the second window of the NIR range, with known advantages in imaging. PLQY values up to 23% have been reported, which are on the same level as Pb(II) QDs, just below Cd(II) QDs. The big advantage that Ag-based NIR QDs have over the other reported materials is their high biocompatibility, even though, technically, Ag is considered a heavy metal (Aydemir et al., 2020). There is still room for improvement with regard to the optical properties and functionalization of the surface, but a translation to clinical applications is on the horizon.

Carbon-based NIR QDS

Carbon QDs (CQDs) have caught the interest of the community after their first synthesis in 2006 during the purification of single-walled carbon nanotubes (Sun et al., 2006). The excellent biological compatibility and low toxicity, coupled with good optical properties and NIR fluorescence, are some of the arguments in favor of their use in biomedical imaging.

There are fundamentally two synthetic approaches for the synthesis of CQDs: top-down and bottom-up. As their names imply, the top-down approach utilizes large carbon precursors, such as nanodiamonds, carbon nanotubes, or carbon fibers and transforms them into smaller particles by the use of physical or chemical processes. These can be laser ablation or oxidation with strong acids or through electrochemical oxidation. Bottom-up approaches imply the fusion of small carbon molecules into larger particles either through

solvothermal or through microwave synthesis. A limitation to the bottom-up synthetic methods is that they generally produce blue- or green-emitting QDs. To increase the relevance of CQDs produced in this manner, there is an ongoing search for different precursors that can be used to produce more relevant, NIR-emitting, CQDs. Despite being a recently developed class of QDs, CQDs have already been applied to several systems and therapies, such as photothermal therapy, photodynamic therapy, and chemical and biological sensing (Ge et al., 2014; Nair et al., 2014; Pang et al., 2020).

CQDs have been synthesized using the microwave synthetic method, through the pyrolysis of glycerine in the presence of polydopamine (Bai et al., 2018). The presence of dopamine allows for a further passivation of the surface of the CQDs and additional nucleation sites provided by the phenolic group. The synthesis is performed in just 5 min, and the PLQY of these CQDs is 5%. The low PLQY is obviously a limitation for their application, but the extreme fast synthesis and biocompatibility supports the investment in further developing this method.

Li and co-workers synthesized NIR-emitting CQDs by combining the solvothermal method and microwave methods (Li et al., 2019b). In a first step, red-emitting CQDs are synthesized by the solvothermal route by mixing citric acid and urea in dimethylformamide (DMF) in an autoclave at 160°C for 6 h. In a second step, the synthesized CQDs were then mixed with DMF and heated by microwave irradiation at 100°C for 70 min at atmospheric pressure. Here, the microwave synthesis acts as an exfoliating method for the graphene-layered red-CQDs. The choice of solvent is important as the DMF, with its electron-accepting carbonyl group, can interact with the carbon skeleton on the pre-formed CQDs and disrupt the layer-staking process. The results are NIR-emitting CQDs with emission peaks at 770 nm and with PLQY of 11%. These nanoparticles show further thermally induced electron transitions that allow for the occurrence of upconverting photoluminescence, without the need to use pulsed laser beams. This allows for a continuous excitation (808 nm) of the CQDs and introduces them as viable *in vivo* NIR probes.

Although carbon is an interesting element to develop probes, given its excellent biological compatibility, the synthesis of CQDs is still in an early stage. The different methods that have been used still need to be optimized, because the emission peaks obtained through hydrothermal and microwave methods barely occur in the NIR-I range, and the PLQYs obtained through these methods generally are lower in comparison to the other materials.

BIOMEDICAL IMAGING APPLICATIONS

The combination of the high resolution and rapid image acquisition of fluorescent imaging, the increased tissue penetration of NIR light, and the optical properties of QDs, yields the opportunity for developing imaging agents that can be used for unique applications. The high photostability of QDs lends itself to applications in which repeated imaging is necessary—for example, tracking of individual cells or image-guided surgery. The nature of nanoparticle surface chemistry allows for the addition of repeated targeting agents to improve affinity, or of secondary ligands (such as PEG chains) to tune the biodistribution, or to incorporate additional modalities to allow for multimodal imaging. The large Stokes shift of QDs also allows for multiplex imaging—imaging of multiple targets with the same excitation wavelength, by monitoring different emission wavelengths—that can allow for imaging multiple different targets, either for simultaneous imaging of different tissue types or for validation/increased specificity of a cell type.

Non-specific targeting

QDs have been applied to various biomedical imaging applications, with and without specific targeting motifs being incorporated.

Pons et al. used ZnCuInSe/ZnS QDs (d = 3–4 nm, $d(hydrodynamic)$ = 9 nm, λ_{em} = 800 nm, $PLQY$ = 20%–30%) to track individual cells *in vivo* through time-gated imaging in the NIR window. By preparing QDs with a fluorescence lifetime (150–300 ns) greater than the observed lifetime of the autofluorescence, the authors were able to collect only the signal from the QDs by waiting for the background signal to decay. Calibration of this delay time (20 ns) in a QD-labeled red blood cell model resulted in rejection of 99% of autofluorescence but retention of 60% of the QD fluorescent signal. The QD-labeled red blood cells were imaged in the blood vessels in the ear of a mouse; by tracking individual cells the velocity in the blood vessels could be measured as being 200–300 $\mu m\ s^{-1}$. Applying the same imaging technique to lymphoma (murine reticulum cell sarcoma) cells in larger blood vessels gave a velocity of approximately 1000 $\mu m\ s^{-1}$ (Pons et al., 2019).

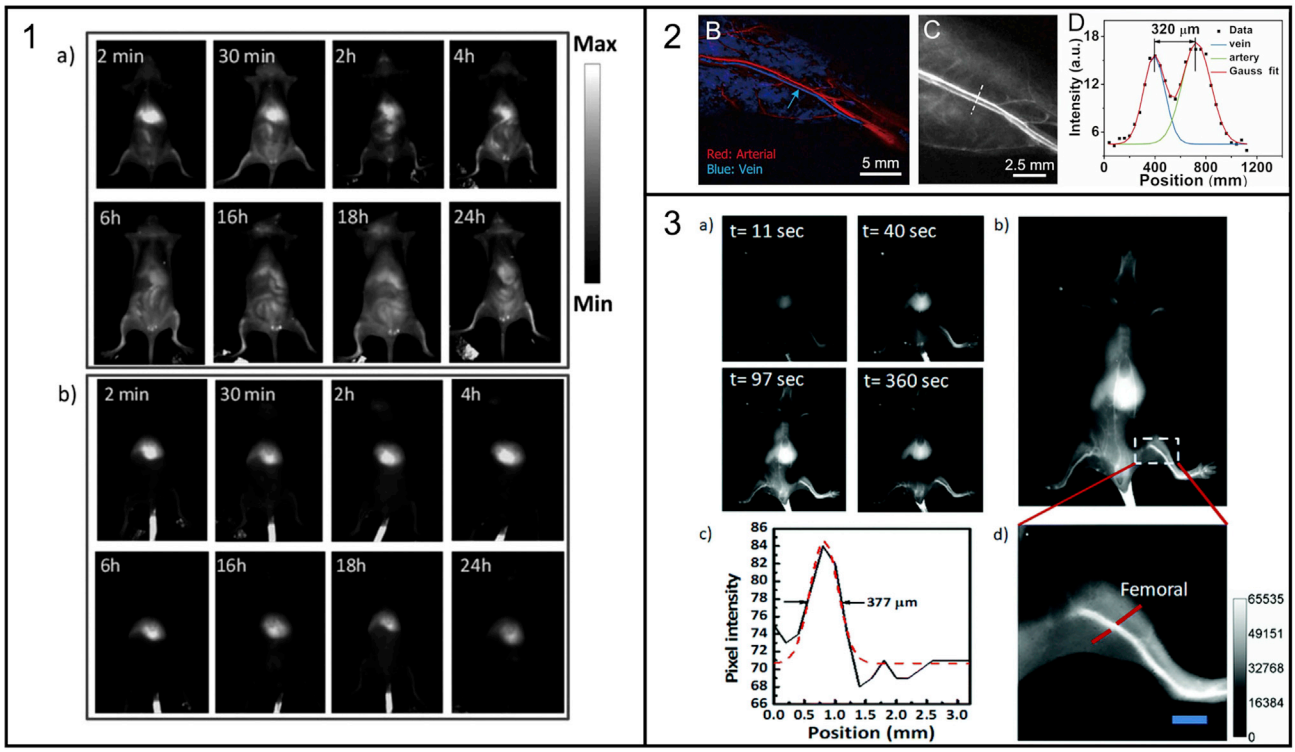

Figure 6. Unspecific targeting of NIR QDs in the imaging of cancer cells and vasculature

Panel 1: *In vivo* tracking of cancer cells. Adapted with permission from (Awasthi et al., 2020). Copyright © 2020, Royal Society of Chemistry.

Panel 2: Femoral artery and vein resolution with separation of 320 μm. Adapted with permission from (Zhang et al., 2018). Copyright © 2019, American Chemical Society.

Panel 3: Long blood-circulating Ag_2S QDs allow for imaging of femoral artery of width 377 μm. Adapted with permission from (Awasthi et al., 2020). Copyright © 2020, Royal Society of Chemistry.

Awasthi et al. used Ag_2S QDs to track metastatic tumor cells in the blood stream. They incubated A549 cancer cells (50,000 cells ml^{-1}) with PEG-PATU coated Ag_2S QDs (100 μM) for 4 h, resulting in an average of 0.296 ng Ag_2S per cell. These cells were then intravenously administered into a mouse and followed by NIR-II emission over 24 h. The fluorescence signal initially appeared in the liver but redistributed across the whole body over the 24-h period (Figure 6, Panel 1a). In contrast, when the same dose of PEG-PATU Ag_2S QDs (14.78 μg mL^{-1} Ag_2S) was administered in healthy controls, the emission remained confined within the liver throughout the experiment (Figure 6, Panel 1b), suggesting that the *in vivo* behavior of the cancer cells could be imaged using this technique (Awasthi et al., 2020).

Awasthi et al. also explored the use of Ag_2S QDs for angiography. By conjugating larger PEG chains (PEG1000) to the Ag_2S QDs they sought to prolong their blood circulation *in vivo*. When applied *via* intravenous injection into a mouse (injected dose = 200 μg Ag_2S) the vascular system of the mouse could be visualized through the NIR-II emission. This yielded high spatial resolution images (femoral artery diameter of 377 μm observed) in "real time" (Awasthi et al., 2020).

Varying the surface coating in this way is an important tool for optimizing the performance of QD-based imaging agents. Changing the coating agent allows for the use of optimized materials for different applications—changing the size, charge, and other targeting properties without significantly altering the optical properties.

Zhang et al. used PbS/CdS QDs (λ_{ex} = 808 nm, λ_{em} = 1650 nm, injected dose = 400 μg PbS/CdS) coated in a branched PEG layer to image blood flow in mouse vasculatures. The QDs had a long blood circulation half-life of 7 h and could be imaged at 60 frames per second through the skin with an exposure time of 2–5 ms. This allowed for resolving the femoral artery and vein at a 320 μm separation at 2 mm depth (Zhang et al., 2018). They were also

used to produce a 3D confocal image of MC38 tumor vasculature (imaging depth 1.2 mm) in live mice, with accumulation attributed to the enhanced permeation and retention (EPR) effect. The accumulation reached a peak at 24 h post-injection, with a tumor to normal tissue ratio of 32.6 (Zhang et al., 2018). The PbS/CdS QDs were shown to be primarily excreted with the feces; with 76% of injected QDs being excreted within 28 days. These excreted QDs were shown to be intact *via* TEM, and no obvious toxicity was seen *in vivo*. However, a significant portion of the injected QDs remained within the mice after 1 month; 0.7% being retained in the liver, spleen, lungs, kidneys, stomach, and gut, with the rest being distributed throughout the body, including in the bones, skin, muscle, and brain. Given the toxic nature of the component materials (Pb(II) and Cd(II)), this long retention is worrying and may hamper future applications despite the apparent high stability.

These two separate studies on the use of NIR QDs for imaging of blood vessels in mice both found similar limits to the lateral resolution—377 μm (Awasthi et al., 2020) and 320 μm (Zhang et al., 2018). This is a fairly high resolution but does not yet approach the limits possible for fluorescence imaging through, for example, confocal microscopy. This is likely due to the inherent constraints of imaging inside an animal versus a single slice of cells but is something that future developments may improve upon.

These examples serve to demonstrate the high spatial and temporal resolution obtainable with NIR QDs. This high-quality imaging data can be acquired rapidly and repeatedly, enabling a greater understanding of rapid processes *in vivo* (Pons et al., 2019). The ability to track cell populations as they are distributed can be used to further understand metastatic cancer (Awasthi et al., 2020; Pons et al., 2019), bacterial infections (Wang et al., 2020), and immune responses (Yu et al., 2019; Yuan et al., 2020), potentially opening new avenues of therapy.

Specific targeting

There are a number of approaches that can be taken to target QDs specifically to disease states. The QDs can have targeting agents added to the surface; this can take the form of small molecules (Ge et al., 2019), peptides (Li et al., 2020; Tang et al., 2015), proteins (Le et al., 2020; Sarkar et al., 2020), or antibodies (Yu et al., 2019). The QDs can also be incorporated into larger systems (Zhang et al., 2019b), such as cell vesicles, that have targeting agents on the surface and act as carriers of the QDs.

Ge et al. used the increased glucose consumption of tumors to target their Ag_2Se QDs. By reacting the pendant carboxylic acids of the coating ligands with glucosamine they added glucose molecules to the surface of the QDs. These showed increased uptake in MCF-7 cells compared with the non-conjugated QDs as assessed by flow cytometry (93.9% of cells labeled versus 4.2%). *In vivo* the glucose-coated QDs showed tumor accumulation in 2 h post-injection and were still detectable after 7 days (Ge et al., 2019). In tumor bearing mice, Ag_2Se QD fluorescence was still observable 7 days post-injection in the kidneys, and in nude mice, Ag could be detected in both the heart (5.41 ± 4.8 μg g^{-1}) and kidneys (113.73 ± 19.00 μg kg^{-1}) 7 days after injection of the glucose-coated Ag_2Se QDs (150 mg kg^{-1} injected dose, 10 times the dose used for imaging experiments), although no significant difference in blood biochemistry was observed over this period.

Tang et al. targeted the $\alpha_v\beta_3$ integrin using a cyclic pentapeptide, cRGDfK, conjugated to the surface of small Ag_2S QDs ($\lambda_{em} = 820$ nm, $d = 6.12 \pm 1.09$ nm, $PLQY = 14.1\%$). This resulted in a probe with an average of 5 peptides per QD; the affinity of this conjugate for $\alpha_v\beta_3$ integrin receptor (2.74 ± 0.94 nM) was shown to be comparable to the peptide on its own (1.42 ± 0.38 nM) and superior to a small molecule analogue (4.29 ± 0.56 nM). When applied *in vitro* the cRGDfK-Ag_2S QDs exhibited intracellular fluorescence within 1 h in mouse breast cancer cell lines (4T1luc), which increased throughout the 24 h of experimental time. The non-conjugated QDs showed negligible internalization in this time frame. Similar internalization patterns were seen in A549 human lung adenocarcinoma epithelial cells. *In vivo* the targeted QDs showed uptake in the tumors after 1 h, again with maximal contrast after 24 h. Based on the *in vivo* imaging results, the authors concluded that the small hydrodynamic size of these QDs results in a similar biodistribution to small organic molecules. However, *ex vivo* analysis of the organs reveals significant uptake in both the kidneys and liver alongside the tumors, with lower uptake in other organs and tissues. This is to be expected as these are the primary excretion routes, but this highlights the importance of validating the observed *in vivo* results further. Tang et al. also highlight the photostability of QDs, with no change in emission intensity observed over 24 h with irradiation from a tungsten lamp or over 30 days in a refrigerator at 4°C and multivalency of this particular design being the benefits of their system (Tang et al., 2015).

Li et al. developed Ag_2S QDs for imaging of traumatic brain injury (TBI). They paired the Ag_2S QDs (λ_{em} = 1050 nm) with an organic dye, A1094, that has absorption overlap with QDs emission (1094 nm), forming a Förster resonance energy transfer (FRET) pair that results in a quenched emission. However, in the presence of peroxynitrite ($ONOO^-$) this dye is oxidized reducing its absorbance at this wavelength and allowing the QD emission to be observed. The pair form a "turn ON" sensor for $ONOO^-$ that was exploited in this work to offer a highly specific and sensitive imaging probe for this biomarker of TBI. The authors compared QDs coated with VCAM1 binding peptide (V@Ag_2S, targeted, always on), A1094 FRET quencher (A@Ag_2S, non-targeted, activatable), and a combination of both (V&A@Ag_2S, targeted and activatable) in a TBI mouse model. They also compared these results with the V&A@Ag_2S probe in a healthy mouse. The results show that without the targeting agent or TBI the QDs do not show any significant uptake in the brain. However, with the targeting agent there is widespread uptake within the brain resulting in a large background signal and the site of injury being difficult to detect. When imaged with the targeted, activatable probe, the injury is apparent, as there is no background signal from the non-injured regions of the brain (Figure 8, Panel 1) (Li et al., 2020).

Through the use of $Hg_xCd_{1-x}Se/Cd_yZn_{1-y}S$ QDs with similar emission profiles (600–700 nm), but different sizes (9.2–17.4 nm hydrodynamic radius), Le et al. delineated the effect of size on the signal-to-noise ratio obtained in three different biological models: live cells, fixed cells, and neuronal synapses. Throughout this work they had to contend with a significant difference in brightness observed for the different-sized nanoparticles due to different absorbance and blinking properties. Despite this, the authors were able to show that the nanoparticle samples that were smaller than 15 nm had superior signal-to-noise ratio due to reduced non-specific uptake, and in the case of the sterically crowded environment of the neuronal synapses only the smallest nanoparticles were able to effectively image the region of interest effectively (Le et al., 2020).

In another study, the same group developed three domain (core)shell/shell $(Hg_xCd_{1-x}Se)Hg_yCd_{1-y}S/Cd_zZn_{1-z}S$ QDs with emission from 630–1360 nm. This range of emission wavelengths was obtained without varying NP size (6 nm) but instead by varying the core composition, with Hg/Cd ratios of 0–0.31. These QDs had similar brightness and PLQY and were again applied to imaging in a variety of biological models. When applied to single QD imaging, the NIR-emitting QDs performed significantly better due to the reduced autofluorescence. Sarkar et al. reported that in this region the autofluorescence was so low as to be indistinguishable from background. This resulted in signal-to-noise ratios (SNR) of 55, whereas for the QDs in the visible range the ratio was 1.6 due to a higher background signal. A similar result was seen when imaging RNA, resulting in an approximately 10-fold improved SNR for the NIR-emitting QD samples compared with the visible region emitting samples. When studying fixed mouse adipose tissues, the autofluorescence was found to be much higher. The visible emitting QDs were not distinguishable from this autofluorescence, but the QDs emitting at 950 and 1130 nm were able to be imaged (SNR ratios of 23 and 29, respectively) allowing for the imaging of alpha tubulin with these probes (Sarkar et al., 2020).

The large Stokes shift of QDs, combined with a broad absorbance spectra, can allow for the design of multiplexing systems in which a single excitation laser can be used to excite two different QD probes. Yu et al. used this property to image myeloid derived suppressor cells (MDSCs) in order to gain further understanding into immune checkpoint blockades to help develop immunotherapy. MDSCs express both CD11b and Gr-1; the authors proposed two-color imaging of both antigens simultaneously to allow for specific imaging of the cells that express both through colocalization of the signal. Yu et al. prepared two different PbS/CdS QDs probes that emit light in the NIR-II window when excited by light at 808 nm: NIR-IIa (d = 4.7 nm, λ_{em} = 1100 nm, *PLQY* = 6.5%) was conjugated to the CD11b-targeting monoclonal antibody ($d(DLS)$ = 41.7 $\pm$ 0.6 nm upon conjugation, ζ = -3.7 ± 0.1 eV) and NIR-IIb (d = 6.8 $\pm$ 0 0.4 nm, λ_{em} = 1600 nm, *PLQY* = 2.3%) conjugated to a Gr-1 monoclonal antibody ($d(DLS)$ = 44.5 $\pm$ 0.6 nm upon conjugation, $\zeta = -2.8 \pm 0.1$ eV). Two-color imaging of a mouse with a SCC7 xenograft showed an increased fluorescence in the tumor, spleen, and lungs for over 72 h (Figure 7)—the control (PbS/CdS QDs with a goat antirabbit IgG antibody conjugated to it) accumulated in the tumor initially before clearing, and no signal was seen in the spleen or lungs after 48 h. The presence of MDSCs in the lungs was confirmed by histological analysis and flow cytometry and the relative abundancy compared with the spleen and tumor validated in relation to the fluorescence. No significant cytotoxicity or *in vivo* toxicity was detected using this probe. This work shows the viability of multiplex imaging within the NIR-II window using QDs and also acts as a demonstration of the use of this technique for targeting a specific subset of cells *in vivo* through the use of complementary antibodies (Yu et al., 2019).

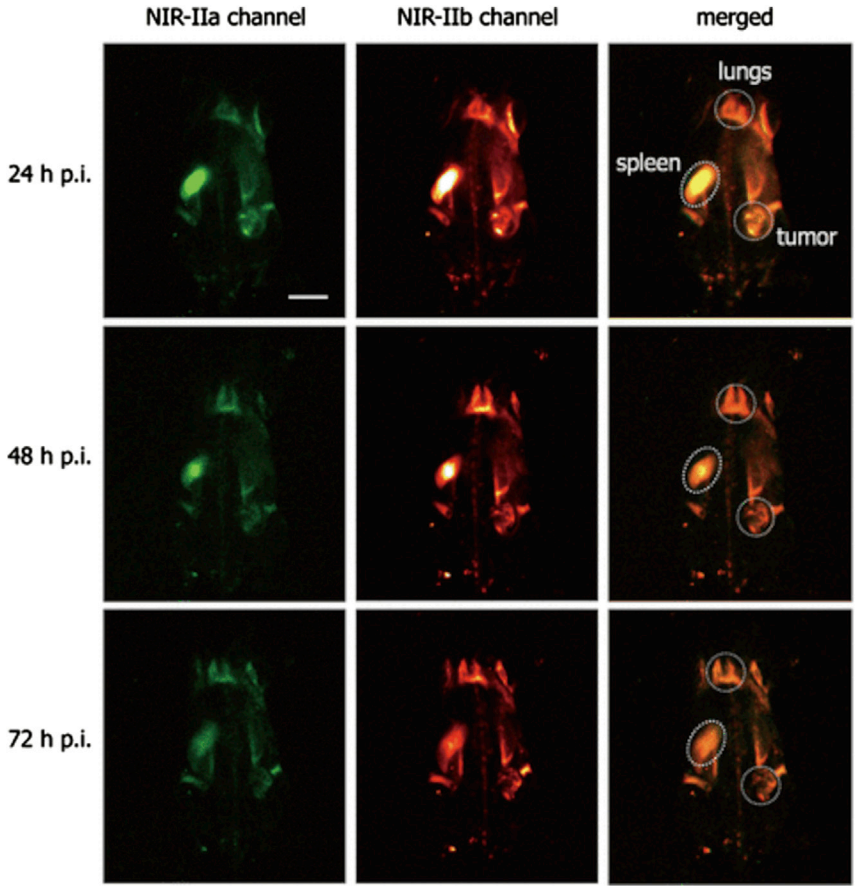

Figure 7. *In vivo* non-invasive two-color fluorescence imaging of mouse possessing SCC7 xenograft in the NIR-II window

The mouse was intravenously injected with the mixture of CD11b@NIR-IIa QDs and Gr-1@NIR-IIb QDs nanoprobes and was imaged at different time points with 808 nm excitation and 980 nm LP plus 1200 nm SP emission filters for NIR-IIa channel and 980 nm LP plus 1500 nm LP emission filters for NIR-IIb channel. Scale bar: 10 mm. Imaging experiment parameters: 1× magnification objective, 808 nm laser, laser power: 20 mW/cm^2, exposure time: 200 ms. Adapted with permission from (Yu et al., 2019).

Zhang et al. compared the effect of different coatings on the tumor uptake of Ag_2Te QDs. Three samples were prepared: PLGA polymer-coated QDs (PQDs), PLGA polymer-coated QDs that had been further coated with PEG (a typical "stealth" coating) (PPQDs), and PLGA polymer-coated QDs contained within a cell vesicle (CV) by extrusion (CPQDs). The CVs were prepared from the cell membranes of 4T1 (mammary breast cancer) cells; these CVs contained a greater CD47, EpCAM, TF-antigen, and E-cadherin protein content than the whole cell lysates, with similar content in both the CVs and CPQDs. The CPQD uptake by macrophages after 4 h was shown to be substantially lower than the non-coated PQDs and slightly less than the traditional PPQDs. The CPQDs were also found to have extended blood retention when injected intravenously into a mouse, with a blood half-life of 7.4 h (1.6 h for PQDs, 6.0 h for PPQDs). Whole-body NIR II fluorescence images of mice with 4T1 tumors that had been injected with either PQDs, PPQDs, or CPQDs over 48 h showed the two "stealth"-coating QDs had increasing fluorescent intensity within the tumor over time (maximum 24 h post injection), whereas the PQDs showed no uptake (Figure 8, Panel 2a). The CPQDs showed the highest fluorescent intensity in the tumors, with tumor/tissue ratio reaching a maximum of 13.3 at 24 h post-injection (Figure 8, Panel 2b). This shows that coating in the membrane of 4T1 cells can be used to target 4T1 tumors as expected, as many of the proteins are "self-targeting." However, the question of whether this can be applied as a generic tumor targeting coating remains, and this may be where the simple PEG coating remains a more effective route to production of generic contrast agents rather than bespoke (Zhang et al., 2019b).

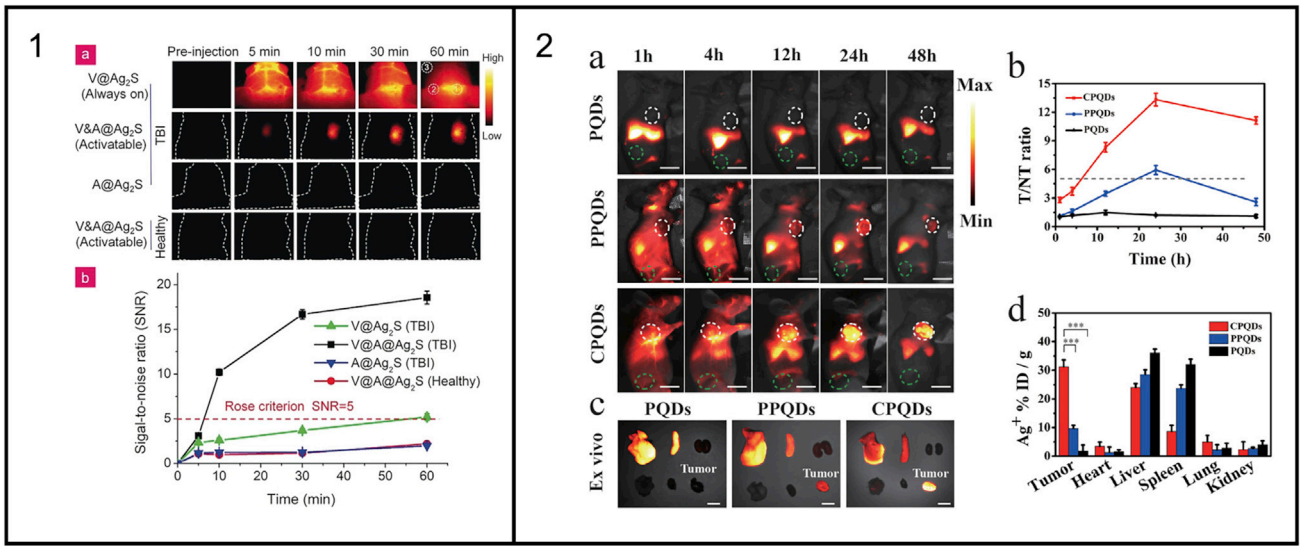

Figure 8. Targeting ability of Ag-based NIR QDs dependent on the surface coating

Panel 1: Demonstration of the use of a "turn-ON" probe to reduce background signal in traumatic brain injury. Adapted with permission from (Li et al., 2020). Copyright © 2019, John Wiley and Sons.

Panel 2: Demonstration of "self-targeting" cell vesicle carriers for enhanced QD localization. Adapted with permission from (Zhang et al., 2019b). Copyright © 2019, John Wiley and Sons.

Image-guided surgery

Image-guided surgery (IGS) involves the use of intraoperative imaging methods to aid the surgeon in performing the surgery. Some preoperative diagnostic methods such as MRI, PET, and SPECT are highly useful in tumor imaging; however, in practice these are difficult to apply during intraoperative procedures. Fluorescence molecular imaging is established as the clinical standard for IGS to aid in the resection of cancers, including breast cancer, head/neck cancers, and lung cancer among other cancers (Mondal et al., 2014). NIR dyes offer advantages over visible dyes in sensitivity as the autofluorescence from biological samples is negligible at NIR wavelengths (Hu et al., 2018). Moreover, the fluorescence emission is highly penetrating and, in most cases, has a long excited-state lifetime. Indocyanine green (ICG) and 5-aminolevulinic acid (5-ALA) are both FDA- and EMA-approved NIR dyes that have been used intraoperatively to carry out tumor resections. The use of ICG to conduct intraoperative tumor resections for breast cancer, skin cancer, and liver cancer has been demonstrated clinically, whereas 5-ALA has primarily been utilized for the resection of malignant gliomas (Schaafsma et al., 2011; Stummer et al., 2006). However, these dyes lack specificity for the target and there are some major issues to tackle, especially for the resection of brain tumors. For example, when using 5-ALA, IGS must be conducted in the dark with low-intensity blue light, which risks damage of healthy brain tissues due to poor illumination. Recent developments of NIR QDs for *in vivo* real-time imaging have shown potential for IGS due to characteristic properties such as brightness, photostability, and low toxicity (Aswathy et al., 2010). Notably, NIR QDs may be conjugated to biologically related components such as peptides and known ligands for specificity of the QDs to its target; hence, the fluorescence is localized at the exact site of resection that minimizes damage to surrounding tissues (Blanco-Canosa et al., 2014).

Over the past two decades, significant research has been published on the topic of NIR QDs for the application of IGS of a range of cancers. Kim and Soltesz et al. were some of the first to publish their work with NIR QDs for the sentinel lymph node (SLN) mapping of the lung and subsequent IGS, which was demonstrated successfully on pigs (Kim et al., 2004; Soltesz et al., 2005). The core/shell CdTe/CdSe NIR QDs (d = 10 nm, λ_{em} = 860 nm, PLQY = 13%) were compared post-injection with a commonly used fluorescent dye, isosulfan blue; here brighter fluorescence and significantly greater tissue penetration in comparison to the dye was observed. Furthermore, only 200 pmol of the QDs was injected compared with 4 mL, 1% isosulfan blue (approx. 70 nmol); this suggests a greater sensitivity and specificity for accurate IGS with a potential to target non-small cell lung cancer (NSCLC) in the future. Similar lymph node mapping and dual IGS on 4T1 breast cancer mice was carried out by Tian et al. using PbS/CdS NIR II QDs (d = 20 nm, λ_{em} = >1500 nm, PLQY = 6%) with an additional NIR II dye, emitting at >1500 nm and between 1100 and 1300 nm, respectively (Tian et al., 2020). QDs were conjugated to anti-CD3 antibodies for a targeted approach. Similar

conclusions of sensitivity, specificity, brightness, and tissue penetration were found superior in comparison to the clinically approved ICG. In addition, a greater photostability than ICG was observed, as there was no photobleaching after 5 h laser exposure, whereas it had only taken several minutes for visible photobleaching in the case of ICG. Hence, this method allows for the feasibility of operating under bright light with continuous laser exposure with a picomolar dose; this is not possible with traditional dyes.

Bioconjugation of CdTe/CdSe/ZnSe NIR QDs to anti-HER2 antibodies was published by Rizvi et al.; however, only *in vitro* experiments were carried out to demonstrate the possibility of IGS of breast cancers. There have been other reports of bioconjugated Cd-based NIR QDs that have been used for *in vitro* selectivity of other cancer cells, including liver cancer (Li et al., 2016), colon cancer, pancreatic cancer, and bladder cancer, suggesting the uses for *in vivo* real-time imaging (Brunetti et al., 2018). However, there have been some concerns regarding the safety of Cd-based NIR QDs, as Cd^{2+} released from the surface of the QDs has known issues of toxicity to cells and tissues. There have been several reports on minimizing the impact of cytotoxicity, including the use of polymeric coatings and other stabilizing ligands on the surface of the Cd-based QD in the context of IGS. *In vivo* toxicity experiments have been conducted on BALB/c mice by Liu et al. to show that the *N*-acetylcysteine (NAC)-capped CdHgTe/CdS/CdZnS QDs ($d = 2.1 \pm 0.6$ nm, $\lambda_{em} = 750$ nm) have no major effects on the behavior of the mice or the histology of tissues (Liu et al., 2018).

With the current limitations of intraoperative fluorescent molecular imaging for brain cancers, there is a significant risk involved with the procedure. NIR QDs have shown potential to tackle these issues in the future and have unique properties such as crossing the blood-brain barrier through carrier-mediated transport of NPs. The concept of cadmium-free, $CuInSe_2$/ZnS NIR QDs has recently been explored to alleviate concerns of toxicity in a sensitive environment such as the brain (Liu et al., 2016). CGKRK peptide was chosen to conjugate to the QDs through PEG for specific targeting of p32 protein receptors overexpressed on tumor endothelial cells. This research indicated a high photostability, specificity in targeting glioblastoma, and minimal toxicity comparable to NIR dyes for IGS purposes. Some initial studies for real-time imaging of glioblastoma tumors (U87MG) by Cai et al. utilized CdTe/ZnS NIR QDs (d = 15-21 nm, λ_{em} = 705 nm) conjugated with cRGD peptides through PEG to bind to the overexpressed $\alpha_v\beta_3$ integrin (Cai and Chen, 2008; Cai et al., 2006). Here, the key finding showed >4-fold SNR increase from the bioconjugated NIR QD compared with the non-conjugated NIR QD 6 h post-injection. This research was the basis of the work by Li et al., where similar CdTe NIR QDs conjugated to cRGD (d = 4.5 nm, λ_{em} = 728 nm, PLQY = 38%) were used to conduct the intraoperative resection of U87MG tumor bearing mice shown in Figure 9, Panel 1.

In contrast to ICG, which is non-specific and of lower quantum efficiency, bioconjugated NIR QDs have shown here a proof of concept for use in image-guided surgery of glioblastoma (Li et al., 2012). A dual-modality imaging approach with the use of Gd-DOTA-Ag_2S NIR II QDs (d = 20 nm, λ_{em} = 1200 nm) has been employed by Li et al. for the purpose of preoperative detection with MRI and intraoperative NIR II image-guided surgery on U87MG positive mice (Li et al., 2015). In this study, ICG was found to give a fluorescence signal-to-noise ratio of up to 37, whereas the NIR II QDs gave a signal-to-noise of up to 334; furthermore, the NIR II QD gave a T_1 relaxivity of 4.9 mM^{-1} s^{-1} and PLQY of 15%. Post-injection, MR signal in the brain tumor peaked at 10 h and showed no changes in the histology of tissues, making it ideal for preoperative detection and subsequent IGS (Figure 9, Panel 2).

NIR QDs have shown promise as superior alternatives to NIR dyes in the application of IGS, given by the ongoing developments. Current research suggests the benefit of brightness, sensitivity, specificity, and photostability will provide a significant advantage in IGS. The active targeting approach through bioconjugation and the ability to be utilized as multimodal agents gives endless possibilities for NIR QDs in preoperative diagnostics and IGS. However, although toxicity concerns are addressed in literature, preclinical studies may not provide the most accurate indication for the use of NIR QDs in clinical trials. In conclusion, NIR QDs have demonstrated a proof-of-concept for IGS of cancers and show potential for clinical use in one day providing a more accurate prognosis and an increase in successful resection of aggressive cancers such as glioblastoma.

MULTIMODAL NIR QDS

Combining multiple, complementary, imaging modalities into a single moiety can be an effective method to produce superior contrast agents. The high resolution and ability to be rapidly acquired make

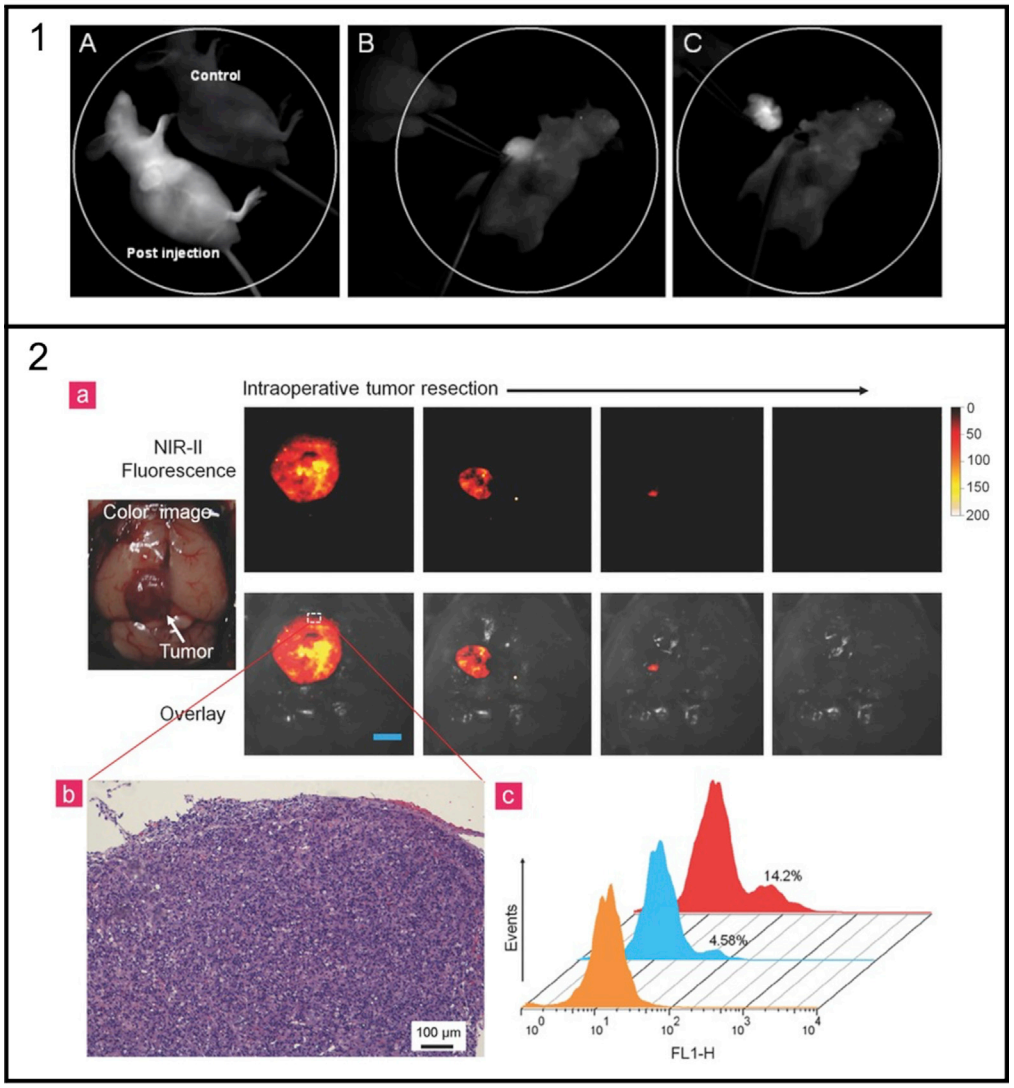

Figure 9. Applications of NIR QDs in image-guided surgery

Panel 1: (A) *In vivo* NIR fluorescence imaging of U87 MG tumor-bearing mice immediately after tail vein injection of cRGD-NIR QD bioconjugates (a non-injected mouse used as blank control); (B) NIR imaging-guided surgery performed 48 h after injection; and (C) the solid tumor precisely removed. Adapted with permission from (Li et al., 2012).

Panel 2: NIR-II fluorescence-guided brain tumor resection using Gd-Ag_2S nanoprobe. (A) U87MG tumor-bearing mice underwent craniotomy under isoflurane general anesthesia, and the tumor was excised step by step (top: NIR-II fluorescence images; bottom: overlay images of brightfield and NIR-II fluorescence). Scale bar represents 2.5 mm. (B) H&E-stained section of excised tumor tissue. (C) Flow cytometric histogram profiles of residual tumor cells. Adapted from with permission from (Li et al., 2015). Copyright © 2015, John Wiley and Sons.

fluorescent imaging a valuable partner for other imaging techniques such as X-rays and MRI (Hemmer et al., 2016). In turn, these modalities can improve the tissue penetration of the probe, allowing for improved diagnosis prior to fluorescence-guided surgery or biopsy sampling.

QDs can be developed into multimodal imaging agents in a number of ways; the surface can be modified with a variety of ligands, or they can be incorporated into larger particles containing other contrast agents (Yang et al., 2019).

Bhardwaj et al. developed silver chalcogenide (Ag_2X, X = S, Se) QDs emitting in the NIR-II region. Following phase transfer, the ligands on the surface of these QDs were substituted for Gd chelates to produce a dual

modal MRI-fluorescence probe. Although they did not report any *in vitro* or *in vivo* applications, the authors demonstrated the increase in MRI contrast agent efficacy that can be expected from this style of multimodal probe; the longitudinal relaxivity increased from 5.36 mM^{-1} s^{-1} (at 400 MHz) for the Gd chelate on its own to 7.75 mM^{-1} s^{-1} and 8.27 mM^{-1} s^{-1} per Gd (at 400 MHz) when attached to the surface of the Ag_2S QDs. The overall relaxivity of the QD-Gd conjugate was recorded to be 407.8 mM^{-1} s^{-1} and 990.3 mM^{-1} s^{-1} per QD (at 400 MHz)—this offers a potentially extremely high relaxivity per target, which will improve the sensitivity of MRI (Bhardwaj et al., 2020).

This approach has proven popular for the development of high relaxivity MRI contrast agents in the past (Stasiuk et al., 2011, 2013) and has the potential to produce effective dual modal contrast agents that can provide both excellent anatomic resolution due to the MRI moiety and molecular concentration sensitivity due to the fluorescent moiety (Bhardwaj et al., 2020). The combination of a small molecule MRI contrast agent into a nanoparticle-based construct in this manner improves the contrast by localizing a high number of contrast agents to increase the local relaxation rate and also by increasing the efficiency of the relaxation achieved by these agents due to a slower rotational correlation coefficient. This effect can be seen by measuring the relaxation rates at multiple magnetic field strengths. Whereas the small molecule probes typically show a decrease in relaxivity around 4 MHz, the nanoparticle-based agents show a distinct increase in relaxivity, with a maxima around 40 MHz, before decreasing again (Stasiuk et al., 2011, 2013). This is particularly useful for the development of clinically relevant agents, as typical clinical MRI scanners operate in the range of 10s–100s of MHz so using QD-based MRI probes will further amplify the contrast gain.

Zhao et al. developed an amorphous $Ag_{2-x}Cu_xS$ system stabilized with BSA that displayed NIR emission, photoacoustic imaging contrast, and photo thermal therapeutic properties. The amorphous nature of these QDs is likely due to the low temperatures and long reaction times of the aqueous, BSA-assisted synthesis. This dual modal imaging probe, combined with its therapeutic properties, produces a "theranostic" agent that can be used for imaging a malady, for treatment, and for monitoring treatment progress. By absorbing light, the $Ag_{2-x}Cu_xS$ nanoparticles can produce heat, causing local hyperthermia and killing the surrounding tissues—ideally the diseased tissue. To reduce the damage to healthy tissues it is important to monitor the photothermal process carefully. The authors desired to include photoacoustic imaging modalities into their theranostic nanoparticle to improve tissue penetration. The particles display a broad absorbance across the visible and NIR range and an emission from 765 to 820 nm upon doping. The PLQY and fluorescence intensity are reduced by doping, limiting the copper content to 1% to retain suitable NIR fluorescent imaging properties. Both NIR fluorescence and photoacoustic imaging could be used to follow uptake of the probe *in vivo* following tail vein injection into a mouse (Figures 10A and 10B). Uptake reached a maximum within the tumor 8 h after intravenous injection, presumably due to the EPR effect. Following a 15-min laser irradiation (635 nm, 0.4 W cm^{-2}), localized temperature increase was observed within the tumor reaching a maximum of 44°C. In the irradiated animals, the volume of the tumors decreased significantly over the 28-day monitoring period when compared with the probe alone or to laser irradiation alone (Figure 10D). The nanoparticles had a long blood circulation half-life of 8.25 h—this allowed for the EPR promoted accumulation with accumulation in the liver, spleen, and lung but gradually decreased from the major organs after 1 day and was low after 7 days but still detectable (Zhao et al., 2020).

CONCLUSIONS AND FUTURE PERSPECTIVES

In this review, we explored the most recent advances in NIR QDs, from synthetic methodologies, materials, and properties to the most recent applications in biomedical imaging and from the heavy metal containing nanoparticles such as Cd(II) or Pb(II) to the most promising Ag(I) and Cu(I) QDs (Table 1). Despite the great advances that have been achieved in order to improve photophysical properties and make the QDs compatible with biological systems, there are still challenges that have to be addressed, such as toxicity, synthetic methodology, biological application, and ability to incorporate other imaging modalities, to allow for the transition of NIR QDs to clinical practice.

a) **Toxicity**: one of the biggest concerns about the utilization of NIR QDs in biological systems is the toxicity associated with the materials of the core. The toxicity and carcinogenic effects of free Cd(II) and Pb(II) ions have been reported (Allocca et al., 2019; Sobhanan et al., 2020)—therefore, there is an inherent risk when using these materials in NIR QDs. Toxicity studies report bioaccumulations in key organs such as liver, spleen, lungs, and kidney for several days following injections. The potential damage to the organism could be fatal if the chemical stability of the QDs is compromised, and although there are shelling strategies, they

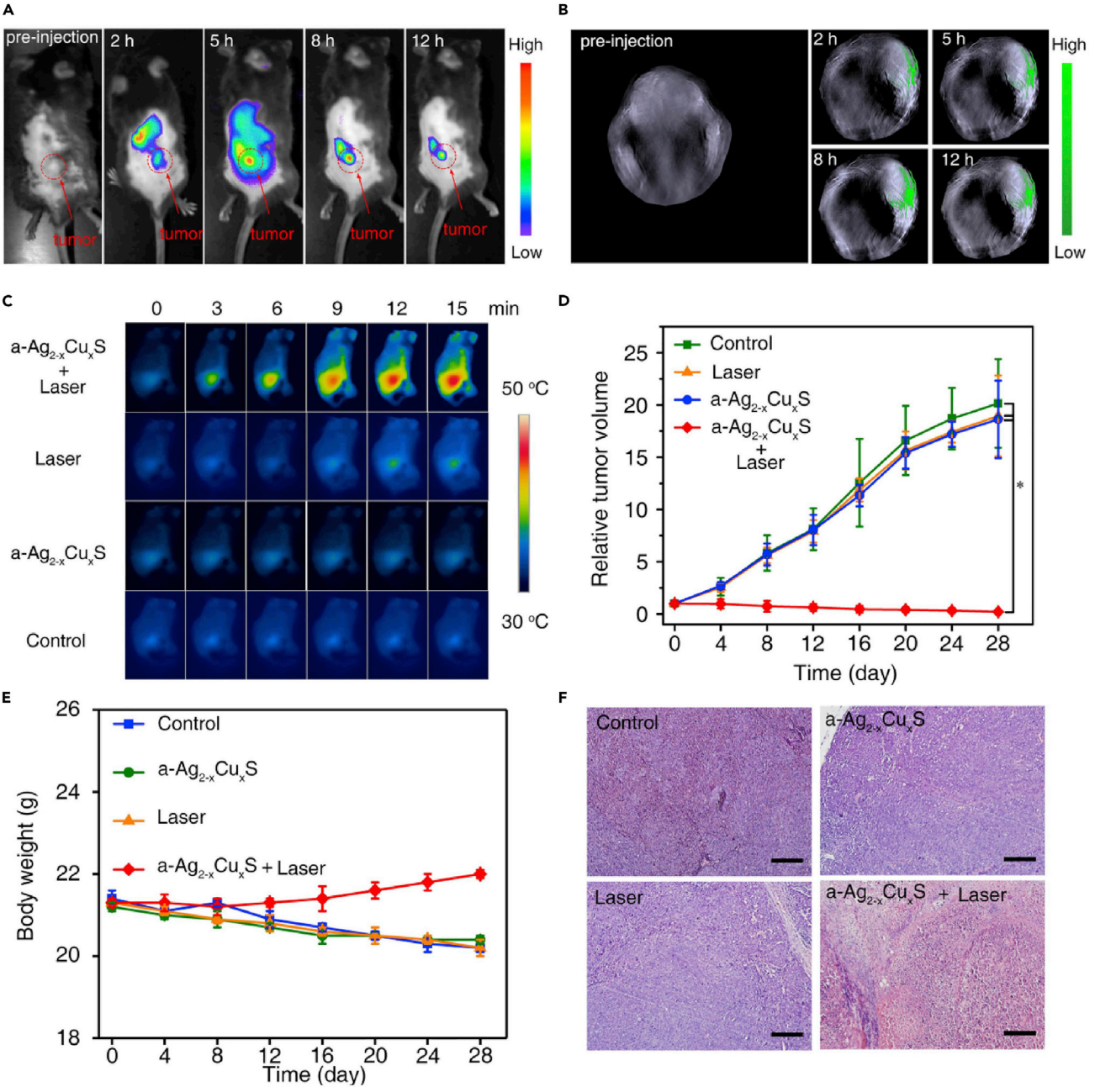

Figure 10. $Ag_{2-x}Cu_xS$ system stabilized with BSA displaying multimodal properties in the NIR range

(A) *In vivo* NIR fluorescence images of a mouse after intravenous injection of a-Ag2-xCuxS QDs acquired at different detecting times under 635 nm irradiation.

(B) *In vivo* PA images of a mouse before and after intravenous injection of a-Ag2-xCuxS QDs.

(C) *In vivo* IR images of mice (tumor sites) under various treatments.

(D) Relative tumor volume change of each group of mice (*p less than 0.05, n = 4).

(E) Body weight change curves of each group of mice (n = 4). (F) Histopathology of tumors with different treatment (scale bar represents 200μm). Adapted from with permission from (Zhao et al., 2020). Copyright © 2020, Elsevier.

do not completely prevent leaching of the core ions. The strategies employed to reduce the leaching of ions from the core involve shelling of the core with other materials such as zinc chalcogenides. Although this strategy is proven to reduce the toxicity (Brunetti et al., 2013), more efficient methods of shelling must be developed to ensure complete encapsulation of the cores and to improve stability. Encapsulation

Table 1. Overview of the most recently synthesized NIR QDS, properties, synthetic methodologies, and biomedical applications

QDs (core/shell)	Surface coating	Emission peak (nm)	Size (nm)	Quantum yield	Synthetic methodology	Biomedical applications	References
CdTe	MPA	700–800	10	15%–20%	Microwave	*In vivo KB* cells tumor targeting	(He et al., 2011)
CdTe/CdS	MPA	710	10	–[a]	Heat-up	Ratiometric biosensor for glucose detection	(Yu et al., 2017)
CdTe/CdS/ZnS	GSH	730	8	45%	Hydrothermal	–[b]	(Samanta et al., 2012)
CdAgS	–[a]	700–800	7.20	36.13%	Non-conventional	–[b]	(Órdenes-Aenishanslins et al., 2020)
CdHgTe	Folate	790	6.68	–[a]	Hydrothermal	*In vivo* tumor imaging	(Chen et al., 2011)
CQDs	–[a]	615	4.54	84%	Hydrothermal	*In vitro* and *in vivo* two-photon imaging with various bio-samples	(Liu et al., 2020b)
CQDs	PDA	–[a]	25	5%	Microwave	Photothermal therapy	(Bai et al., 2018)
CQDs	–[a]	770	2–6	11%	Microwave	NIR up conversion luminescence imaging *in vivo*	(Li et al., 2019b)
CQDs	Chlorin e6	632–653	9.9	–[a]	Hydrothermal	Photothermal/photodynamic synergistic cancer therapy	(Sun et al., 2019)
PbS	MUA	1100	7.5 ± 2.5	8%	Hot-injection	Imaging of the thrombotic state in septic brain	(Imamura et al., 2016)
PbS/CdS	anti-CD3 antibody	1600	17.1	~6%	Hot-injection	Imaging-guided lymph node surgery	(Tian et al., 2020)
PbS/CdS	PEG	1600	18.2	2.2%–22%	Hot-injection	*In vivo* confocal 3D imaging of tumor vasculature	(Zhang et al., 2018)
PbS/CdS/ZnS	MPA	930-1220	5.7–6.2	30%–20%	Hot-injection + Microwave	*In vivo* tumor imaging	(Ren et al., 2017)
Ag_2S	Gd chelates	1200	4.2	6%	Heat-up	Dual-modal MRI/NIR imaging of brain tumors	(Bhardwaj et al., 2020)
Ag_2S	PEG	1135	8	–[a]	Hydrothermal	Tracking of cerebral vascular anomalies	(Parchur et al., 2020)
Ag_2S	PEG-PATU	1100	25–30	7.8%	Hydrothermal	*In vivo* imaging of the vasculature system	(Awasthi et al., 2020)
Ag_2S	cRGDfK	500–1200	1.5–9	4.4%–22.7%	Hydrothermal	Integrin-targeted tumor imaging	(Tang et al., 2015)
Ag_2Se	Glucose	~775	2.4 ± 0.5	3.1%	Non-conventional	*In vivo* long-term observation of tumor evolution	(Ge et al., 2019)
Ag_2Te	PLGA	1300	106 ± 2	2.3%	Hot-injection	*In vivo* Homotypic tumor imaging	(Zhang et al., 2019b)
Ag_2Te/Ag_2S	PEG	1560	5.71	4.3%	Hot-injection	Imaging of deep organs and vascular structure	(Zhang et al., 2020)
$CuInS_2/ZnS$	MUA	1050	9.2 ± 0.6	6.0%	Hot-injection	–[b]	(Xia et al., 2017)

Reported optical properties of the NIR QDs (emission, size, PLQY) refer to the QDs with the surface modification and in aqueous media

Abbreviations: MPA, mercaptopropionic acid; GSH, glutathione; PDA, polydopamine; MUA, mercaptoundecanoic acid; PEG, polyethylene glycol; PATU, polythiourea dendrimer; PLGA, poly(lactic-co-glycolic acid).

[a]These data have not been disclosed by the authors of the study. In the case of CQDs, most synthesis do not report a surface coating given the as-synthesized biocompatibility

[b]These NIR QDs do not possess reported preclinical applications.

of the QDs with silica polymers is another strategy used to prevent the leaching of toxic elements. Functional organosilicon molecules are grafted onto the surface *via* -NH_2 or -SH groups and provide additional biocompatibility. The main challenges associated with silica coating are the difficulty in controlling the thickness of the shell, often yielding larger QDs, with the PLQY usually decreasing after coating and the emission peak suffering a blueshift in comparison with core only QDs (Du et al., 2016; Yang et al., 2010). Although it has potential in improving core stability and biocompatibility, optimized silica coating methodologies still have to be developed.

Ag(I) and Cu(I), although being recent developments in NIR QDs, have quickly reached good optical properties when compared with the more studied materials above, with emissions reaching NIR-II windows. The low toxicity and improved biocompatibility (Aydemir et al., 2020; Vardar et al., 2018) of these materials have been the main drive for a gradual research shift toward these NIR QDs. This shift is clear by the growing number of preclinical studies recently published, with this material highlighting the excellent NIR emission and PLQY, good chemical stability, and biocompatibility. Carbon-based NIR QDs while receiving much attention because of the almost inexistent toxicity, still fall far behind of the other described materials. The methods used for the synthesis yield QDs that have difficulties finding the NIR-I window, and the reported PLQY are lower in comparison with Ag(I) or Cu(I) NIR QDs.

For the future, synthetic procedures should focus on Ag(I) and Cu(I) NIR QDs to yield more biocompatible NIR QDs without compromising the optical properties.

b) Synthesis: the synthetic methodologies are the key to tuning NIR QDs optical properties. Despite continuous advances in this area, synthetic methods that yield NIR QDs in aqueous media with high biocompatibility still present weaker fluorescence properties. The hot-injection and heat-up methods are still the most used procedures because they yield QDs with higher PLQY and chemical stability. The synthesized QDs are in organic media; to make them biologically compatible they must undergo phase transfer and/or ligand exchange protocols. The current procedures for performing these steps reduce the PLQY and hinders emission in the NIR region.

The material coating has also shown to be one essential consideration in the synthesis of NIR QDs for biological targeting. Coating with PEG chains of various sizes is the most used approach; the non-specific targeting nature of these molecules has enabled the tracking of individual blood cells or metastatic tumor cells and in the future can be a viable tool to detect bacterial infections or immune responses. More specific targeting molecules have been incorporated into QDs, such as antibodies or peptides, and these allow for increased uptake, and longer retention, of the QDs in target tissues allowing for an increased signal-to-noise ratio (SNR) to be obtained, thus improving image quality.

As challenges for the future, more efficient hydrothermal or microwave routes need to be designed to make the synthesis as consistent as the standard hot-injection methodology, with a focus on one-pot reactions for QDs in aqueous media. In the same sense, the phase transfer protocols can also be further optimized with QDs obtained from hot injection and heat up methods, to improve PLQY.

c) Biomedical applications: NIR QDs have been used to guide therapies—through diagnosis, image-guided surgery, and theranostic applications. One of the most promising applications of NIR QDs is imaging-guided surgery (IGS) due to the higher tissue penetration, PLQY, and photostability, which other NIR molecular probes lack. The specificity of these probes allows for a more selective excision of the affected tissue while minimizing the damage to the surrounding healthy tissue. Pre-clinical studies have been conducted, testing the application of NIR QDs for the IGS of several tissues, such as sentinel lymph node, breast cancer, and glioblastoma. The results are encouraging for NIR QDs as they successfully enabled the removal of the targeted tumor. When in direct comparison with clinically used dyes, such as ICG or 5-ALA, NIR QDs enable the surgeon to clearly distinguish the affected area from the background as a result of the higher SNR.

NIR QDs have also been used in theranostic applications. Current theranostic applications include photothermal therapy, taking advantage of the charge/electron transfers in the emission of NIR fluorescence to destroy target tumors. The main challenge for the future would be to develop QDs with high specificity for each disease, through engineering of the QDs surface, which would be an improvement to the existing non-specific ICG and 5-ALA dyes.

d) Multimodal QDs: the development of multimodal approaches that combine the benefits of fluorescence with other imaging modalities is one of the most promising developments for the future of NIR QDs. Coupling MRI agents to NIR QDs has been reported successfully (Bhardwaj et al., 2020; Ma et al., 2018). Nonetheless, the difference in sensitivity of both techniques implies that a high ratio of MRI contrast agent to fluorescent probe would be beneficial. This can be achieved with QDs; a high number of MRI contrast agents can be loaded onto the surface of each QD. PET has also been paired with fluorescent imaging, benefiting from the high tissue penetration of PET and high resolution of fluorescence imaging. One of the limitations of multimodal imaging is the use of different equipment to detect the reporting mechanisms at the same time. One of the challenges would be the optimization of the concentration of each individual imaging agent in the multimodal probe. Currently, trimodal probes such as NIR fluorescent imaging/MRI/PET have yet to be developed and would be a welcome addition to multimodal imaging, given the potential to explore this synergetic technique.

The list of materials for the synthesis of NIR QDs is varied (Table 1), and the field will benefit from an investment in less-toxic alternatives, replacing the more well-studied materials. With the focus on the improvement of the synthetic methodologies, this would allow for the synthesis of materials with improved and controlled properties, such as size dispersion, NIR emission peak, and PLQY. The improvement of the shelling and surface coating procedures will improve the chemical stability of the cores, addressing the toxicity concerns that QDs still face and improving the clearance of these nanoparticles from the organism. After addressing these core issues, these improved NIR QDs will replace the Cd and Pb materials, and then they will be able to make the transition from the preclinical to a clinical setting, creating new tools for diagnosis and treatment of several diseases.

ACKNOWLEDGMENTS

The authors would like to thank the Medical Research Council for financial support (MR/T002573/1) and also the Engineering and Physical Sciences Research Council (EP/R513064/1) for KC's PhD Studentship.

AUTHOR CONTRIBUTIONS

HG, TWP, and KC drafted the manuscript. GJS, SC, and JSB edited and finalized. GJS conceptualized the idea.

DECLARATION OF INTERESTS

The authors declare no competing interests.

REFERENCES

Alkhybari, E.M., McEntee, M.F., Brennan, P.C., Willowson, K.P., Hogg, P., and Kench, P.L. (2018). Determining and updating pet/ct and spect/ct diagnostic reference levels: a systematic review. Radiat. Prot. Dosimetry *182*, 532–545.

Allocca, M., Mattera, L., Bauduin, A., Miedziak, B., Moros, M., De Trizio, L., Tino, A., Reiss, P., Ambrosone, A., and Tortiglione, C. (2019). An integrated multilevel analysis profiling biosafety and toxicity induced by indium-and cadmium-based quantum dots in vivo. Environ. Sci. Technol. *53*, 3938–3947.

Aswathy, R.G., Yoshida, Y., Maekawa, T., and Kumar, D.S. (2010). Near-infrared quantum dots for deep tissue imaging. Anal. Bioanal. Chem. *397*, 1417–1435.

Awasthi, P., An, X., Xiang, J., Kalva, N., Shen, Y., and Li, C. (2020). Facile synthesis of noncytotoxic pegylated dendrimer encapsulated silver sulfide quantum dots for nir-ii biological imaging. Nanoscale *12*, 5678–5684.

Aydemir, D., Hashemkhani, M., Acar, H.Y., and Ulusu, N.N. (2020). Evaluation of the biocompatibility of the gsh-coated Ag2S quantum dots in vitro: a perfect example for the non-toxic optical probes. Mol. Biol. Rep. *47*, 4117–4129.

Bai, Y., Zhang, B., Chen, L., Lin, Z., Zhang, X., Ge, D., Shi, W., and Sun, Y. (2018). Facile one-pot synthesis of polydopamine carbon dots for photothermal therapy. Nanoscale Res. Lett. *13*, 1–9.

Bhardwaj, K., Pradhan, S., Basel, S., Clarke, M., Brito, B., Thapa, S., Roy, P., Borthakur, S., Saikia, L., Shankar, A., et al. (2020). Tunable nir-ii emitting silver chalcogenide quantum dots using thio/selenourea precursors: preparation of mri/nir-ii multimodal imaging agent. Dalton Trans. *49*, 15425–15432.

Blanco-Canosa, J.B., Wu, M., Susumu, K., Petryayeva, E., Jennings, T.L., Dawson, P.E., Algar, W.R., and Medintz, I.L. (2014). Recent progress in the bioconjugation of quantum dots. Coord. Chem. Rev. *263-264*, 101–137.

Brunetti, J., Riolo, G., Gentile, M., Bernini, A., Paccagnini, E., Falciani, C., Lozzi, L., Scali, S., Depau, L., Pini, A., et al. (2018). Near-infrared quantum dots labelled with a tumor selective tetrabranched peptide for in vivo imaging. J. Nanobiotechnology *16*, 21.

Brunetti, V., Chibli, H., Fiammengo, R., Galeone, A., Malvindi, M.A., Vecchio, G., Cingolani, R., Nadeau, J.L., and Pompa, P.P. (2013). InP/ZnS as a safer alternative to CdSe/ZnS core/shell quantum dots: in vitro and in vivo toxicity assessment. Nanoscale *5*, 307–317.

Buhro, W.E., and Colvin, V.L. (2003). Shape matters. Nat. Mater. *2*, 138–139.

Butson, J.D., Narangari, P.R., Lysevych, M., Wong-Leung, J., Wan, Y., Karuturi, S.K., Tan, H.H., and Jagadish, C. (2019). InGaAsp as a promising narrow band gap semiconductor for photoelectrochemical water splitting. ACS Appl. Mater. Interface *11*, 25236–25242.

Cai, W., and Chen, X. (2008). Preparation of peptide-conjugated quantum dots for tumor vasculature-targeted imaging. Nat. Protoc. *3*, 89–96.

Cai, W., Shin, D.W., Chen, K., Gheysens, O., Cao, Q., Wang, S.X., Gambhir, S.S., and Chen, X. (2006). Peptide-labeled near-infrared quantum

dots for imaging tumor vasculature in living subjects. Nano Lett. *6*, 669–676.

Cao, H., Yue, Z., Gao, H., Chen, C., Cui, K., Zhang, K., Cheng, Y., Shao, G., Kong, D., and Li, Z. (2019). In vivo real-time imaging of extracellular vesicles in liver regeneration via aggregation-induced emission luminogens. ACS Nano *13*, 3522–3533.

Chen, H., Li, L., Cui, S., Mahounga, D., Zhang, J., and Gu, Y. (2011). Folate conjugated CdHgTe quantum dots with high targeting affinity and sensitivity for in vivo early tumor diagnosis. J. Fluoresc. *21*, 793–801.

Chen, S., Ahmadiantehrani, M., Zhao, J., Zhu, S., Mamalis, A.G., and Zhu, X. (2016). Heat-up synthesis of Ag–In–S and Ag–In–S/ZnS nanocrystals: effect of indium precursors on their optical properties. J. Alloys Compd. *665*, 137–143.

Clarke, M.T., Viscomi, F.N., Chamberlain, T.W., Hondow, N., Adawi, A.M., Sturge, J., Erwin, S.C., Bouillard, J.-S.G., Tamang, S., and Stasiuk, G.J. (2019). Synthesis of super bright indium phosphide colloidal quantum dots through thermal diffusion. Commun. Chem. *2*, 1–7.

Cui, Y., Zhang, C., Song, L., Yang, J., Hu, Z., and Liu, X. (2018). Facile synthesis of near-infrared emissive cds quantum dots for live cells imaging. J. Nanosci. Nanotechnol. *18*, 2271–2277.

Dang, X., Bardhan, N.M., Qi, J., Gu, L., Eze, N.A., Lin, C.-W., Kataria, S., Hammond, P.T., and Belcher, A.M. (2019). Deep-tissue optical imaging of near cellular-sized features. Sci. Rep. *9*, 1–12.

Du, Y., Xu, B., Fu, T., Cai, M., Li, F., Zhang, Y., and Wang, Q. (2010). Near-infrared photoluminescent Ag2S quantum dots from a single source precursor. J. Am. Chem. Soc. *132*, 1470–1471.

Du, Y., Yang, P., Matras-Postolek, K., Wang, J., Che, Q., Cao, Y., and Ma, Q. (2016). Low toxic and highly luminescent CdSe/$Cd_xZn_{1-x}S$ quantum dots with thin organic sio 2 coating for application in cell imaging. J. Nanopart. Res. *18*, 37.

Elibol, E. (2020). Synthesis of near unity photoluminescence cdsete alloyed quantum dots. J. Alloys Compd. *817*, 152726.

Gallardo Benavente, C.D., Carrión, O., Todd, J.D., PIERETTI, J., SEABRA, A., DURAN, N., Rubilar, O., Perez-Donoso, J.M., and QUIROZ, A.E. (2019). Biosynthesis of cds quantum dots mediated by volatile sulfur compounds released by antarctic pseudomonas fragi. Front. Microbiol. *10*, 1866.

Ge, J., Lan, M., Zhou, B., Liu, W., Guo, L., Wang, H., Jia, Q., Niu, G., Huang, X., and Zhou, H. (2014). A graphene quantum dot photodynamic therapy agent with high singlet oxygen generation. Nat. Commun. *5*, 1–8.

Ge, X.-L., Huang, B., Zhang, Z.-L., Liu, X., He, M., Yu, Z., Hu, B., Cui, R., Liang, X.-J., and Pang, D.-W. (2019). Glucose-functionalized near-infrared ag 2 se quantum dots with renal excretion ability for long-term in vivo tumor imaging. J. Mater. Chem. B *7*, 5782–5788.

He, Y., Zhong, Y., Su, Y., Lu, Y., Jiang, Z., Peng, F., Xu, T., Su, S., Huang, Q., and Fan, C. (2011). Water-dispersed near-infrared-emitting quantum dots of ultrasmall sizes for in vitro and in vivo imaging. Angew. Chem. *123*, 5813–5816.

Hemmer, E., Benayas, A., Légaré, F., and Vetrone, F. (2016). Exploiting the biological windows: current perspectives on fluorescent bioprobes emitting above 1000 nm. Nanoscale Horiz *1*, 168–184.

Hong, G., Robinson, J.T., Zhang, Y., Diao, S., Antaris, A.L., Wang, Q., and Dai, H. (2012). In vivo fluorescence imaging with Ag2S quantum dots in the second near-infrared region. Angew. Chem. Int. Ed. *51*, 9818–9821.

Hu, S., Kang, H., Baek, Y., El Fakhri, G., Kuang, A., and Choi, H.S. (2018). Real-time imaging of brain tumor for image-guided surgery. Adv. Healthc. Mater. *7*, e1800066.

Huang, J., Xie, C., Zhang, X., Jiang, Y., Li, J., Fan, Q., and Pu, K. (2019). Renal-clearable molecular semiconductor for second near-infrared fluorescence imaging of kidney dysfunction. Angew. Chem. Int. Ed. *58*, 15120–15127.

Imamura, Y., Yamada, S., Tsuboi, S., Nakane, Y., Tsukasaki, Y., Komatsuzaki, A., and Jin, T. (2016). Near-infrared emitting pbs quantum dots for in vivo fluorescence imaging of the thrombotic state in septic mouse brain. Molecules *21*, 1080.

Jagtap, A.M., Chatterjee, A., Banerjee, A., Pendyala, N.B., and Rao, K.K. (2016). Size and temperature dependence of the photoluminescence properties of nir emitting ternary alloyed mercury cadmium telluride quantum dots. J. Phys. D *49*, 135302.

Jain, P.K., Huang, X., El-Sayed, I.H., and El-Sayed, M.A. (2008). Noble metals on the nanoscale: optical and photothermal properties and some applications in imaging, sensing, biology, and medicine. Acc. Chem. Res. *41*, 1578–1586.

Jamieson, T., Bakhshi, R., Petrova, D., Pocock, R., Imani, M., and Seifalian, A.M. (2007). Biological applications of quantum dots. Biomaterials *28*, 4717–4732.

Judenhofer, M.S., Wehrl, H.F., Newport, D.F., Catana, C., Siegel, S.B., Becker, M., Thielscher, A., Kneilling, M., Lichy, M.P., and Eichner, M. (2008). Simultaneous pet-mri: a new approach for functional and morphological imaging. Nat. Med. *14*, 459–465.

Kays, J.C., Saeboe, A.M., Toufanian, R., Kurant, D.E., and Dennis, A.M. (2020). Shell-free copper indium sulfide quantum dots induce toxicity in vitro and in vivo. Nano Lett. *20*, 1980–1991.

Kershaw, S.V., Susha, A.S., and Rogach, A.L. (2013). Narrow bandgap colloidal metal chalcogenide quantum dots: synthetic methods, heterostructures, assemblies, electronic and infrared optical properties. Chem. Soc. Rev. *42*, 3033–3087.

Kim, J.-h., Kim, H.-R., Lee, B.-R., Choi, E.-S., In, S.-I., and Kim, E. (2015). Carcinogenic activity of pbs quantum dots screened using exosomal biomarkers secreted from hek293 cells. Int. J. Nanomedicine *10*, 5513.

Kim, S., Lim, Y.T., Soltesz, E.G., De Grand, A.M., Lee, J., Nakayama, A., Parker, J.A., Mihaljevic, T., Laurence, R.G., Dor, D.M., et al. (2004). Near-infrared fluorescent type II quantum dots for sentinel lymph node mapping. Nat. Biotechnol. *22*, 93–97.

Kubicek-Sutherland, J.Z., Makarov, N.S., Stromberg, Z.R., Lenz, K.D., Castañeda, C., Mercer, A.N., Mukundan, H., McDaniel, H., and Ramasamy, K. (2020). Exploring the biocompatibility of near-IR $CuInSe_xS_{2-x}$/ZnS quantum dots for deep-tissue bioimaging. ACS Appl. Bio Mater. *3*, 8567–8574.

Le, P., Vaidya, R., Smith, L.D., Han, Z., Zahid, M.U., Winter, J., Sarkar, S., Chung, H.J., Perez-Pinera, P., and Selvin, P.R. (2020). Optimizing quantum dot probe size for single-receptor imaging. ACS Nano *14*, 8343–8358.

Leigh, P.N., Simmons, A., Williams, S., Williams, V., Turner, M., and Brooks, D. (2002). Imaging: Mrs/mri/pet/spect: Summary. Amyotroph. Lateral Scler. Other Mot. Neuron Disord *3*, S75–S80.

Li, C., Cao, L., Zhang, Y., Yi, P., Wang, M., Tan, B., Deng, Z., Wu, D., and Wang, Q. (2015). Preoperative detection and intraoperative visualization of brain tumors for more precise surgery: a new dual-modality mri and nir nanoprobe. Small *11*, 4517–4525.

Li, C., Li, W., Liu, H., Zhang, Y., Chen, G., Li, Z., and Wang, Q. (2020). An activatable nir-ii nanoprobe for in vivo early real-time diagnosis of traumatic brain injury. Angew. Chem. *132*, 253–258.

Li, C., and Wu, P. (2019a). Cu-doped quantum dots: a new class of near-infrared emitting fluorophores for bioanalysis and bioimaging. Luminescence *34*, 782–789.

Li, D., Liang, C., Ushakova, E.V., Sun, M., Huang, X., Zhang, X., Jing, P., Yoo, S.J., Kim, J.G., and Liu, E. (2019b). Thermally activated upconversion near-infrared photoluminescence from carbon dots synthesized via microwave assisted exfoliation. Small *15*, 1905050.

Li, Y., Bai, G., Zeng, S., and Hao, J. (2019c). Theranostic carbon dots with innovative nir-ii emission for in vivo renal-excreted optical imaging and photothermal therapy. ACS Appl. Mater. Interface *11*, 4737–4744.

Li, Y., Li, Z., Wang, X., Liu, F., Cheng, Y., Zhang, B., and Shi, D. (2012). In vivo cancer targeting and imaging-guided surgery with near infrared-emitting quantum dot bioconjugates. Theranostics *2*, 769.

Li, Z., Zhang, Q., Huang, H., Ren, C., Pan, Y., Wang, Q., and Zhao, Q. (2016). Rgds-conjugated CdSeTe/CdS quantum dots as near-infrared fluorescent probe: preparation, characterization and bioapplication. J. Nanopart Res. *18*, 373.

Lin, T.Y., Lian, Z.J., Yao, C.X., Du, Q.Q., Liao, S.H., and Wu, S.M. (2020). A rapid biosynthesis of fluorescent cdse qds in bacillus licheniformis and correlative bacterial antibiotic change assess during the process. Luminescence. https://doi.org/10.1002/bio.3980.

Liu, J., Raveendran, P., Shervani, Z., and Ikushima, Y. (2004). Synthesis of Ag2S quantum dots in water-in-co 2 microemulsions. Chem. Commun. 2582–2583.

Liu, X., Braun, G.B., Zhong, H., Hall, D.J., Han, W., Qin, M., Zhao, C., Wang, M., She, Z.G., Cao, C.,

et al. (2016). Tumor-targeted multimodal optical imaging with versatile cadmium-free quantum dots. Adv. Funct. Mater. *26*, 267–276.

Liu, X., Zhou, P., Liu, H., Zhan, H., Zhang, Q., Zhao, Y., and Chen, Y. (2018). Design of bright near-infrared-emitting quantum dots capped with different stabilizing ligands for tumor targeting. RSC Adv. *8*, 4221–4229.

Liu, H., Li, C., Qian, Y., Hu, L., Fang, J., Tong, W., Nie, R., Chen, Q., and Wang, H. (2020a). Magnetic-induced graphene quantum dots for imaging-guided photothermal therapy in the second near-infrared window. Biomaterials *232*, 119700.

Liu, Y., Gou, H., Huang, X., Zhang, G., Xi, K., and Jia, X. (2020b). Rational synthesis of highly efficient ultra-narrow red-emitting carbon quantum dots for NIR-II two-photon bioimaging. Nanoscale *12*, 1589–1601.

Ma, J.-J., Yu, M.-X., Zhang, Z., Cai, W.-G., Zhang, Z.-L., Zhu, H.-L., Cheng, Q.-Y., Tian, Z.-Q., and Pang, D.-W. (2018). Gd-dtpa-coupled Ag2Se quantum dots for dual-modality magnetic resonance imaging and fluorescence imaging in the second near-infrared window. Nanoscale *10*, 10699–10704.

Mondal, S.B., Gao, S., Zhu, N., Liang, R., Gruev, V., and Achilefu, S. (2014). Real-time fluorescence image-guided oncologic surgery. Adv. Cancer Res. *124*, 171–211.

Murray, C., Norris, D.J., and Bawendi, M.G. (1993). Synthesis and characterization of nearly monodisperse CdE (E= sulfur, selenium, tellurium) semiconductor nanocrystallites. J. Am. Chem. Soc. *115*, 8706–8715.

Murray, C.B., Sun, S., Gaschler, W., Doyle, H., Betley, T.A., and Kagan, C.R. (2001). Colloidal synthesis of nanocrystals and nanocrystal superlattices. IBM J. Res. Dev. *45*, 47–56.

Nair, L.V., Nagaoka, Y., Maekawa, T., Sakthikumar, D., and Jayasree, R.S. (2014). Quantum dot tailored to single wall carbon nanotubes: a multifunctional hybrid nanoconstruct for cellular imaging and targeted photothermal therapy. Small *10*, 2771–2775.

Órdenes-Aenishanslins, N., Anziani-Ostuni, G., Monrás, J.P., Tello, A., Bravo, D., Toro-Ascuy, D., Soto-Rifo, R., Prasad, P.N., and Pérez-Donoso, J.M. (2020). Bacterial synthesis of ternary cdsag quantum dots through cation exchange: tuning the composition and properties of biological nanoparticles for bioimaging and photovoltaic applications. Microorganisms *8*, 631.

Pang, W., Jiang, P., Ding, S., Bao, Z., Wang, N., Wang, H., Qu, J., Wang, D., Gu, B., and Wei, X. (2020). Nucleolus-targeted photodynamic anticancer therapy using renal-clearable carbon dots. Adv. Healthc. Mater. *9*, 2000607.

Parchur, A.K., Fang, Z., Jagtap, J.M., Sharma, G., Hansen, C., Shafiee, S., Hu, W., Miao, Q.R., and Joshi, A. (2020). Nir-ii window tracking of hyperglycemia induced intracerebral hemorrhage in cerebral cavernous malformation deficient mice. Biomater. Sci. *8*, 5133–5144.

Peng, Z.A., and Peng, X. (2001). Formation of high-quality CdTe, CdSe, and CdS nanocrystals using CdO as precursor. J. Am. Chem. Soc. *123*, 183–184.

Pons, T., Bouccara, S., Loriette, V., Lequeux, N., Pezet, S., and Fragola, A. (2019). In vivo imaging of single tumor cells in fast-flowing bloodstream using near-infrared quantum dots and time-gated imaging. ACS Nano *13*, 3125–3131.

Pradhan, N., Das Adhikari, S., Nag, A., and Sarma, D. (2017). Luminescence, plasmonic, and magnetic properties of doped semiconductor nanocrystals. Angew. Chem. Int. Ed. *56*, 7038–7054.

Reiss, P., Carriere, M., Lincheneau, C., Vaure, L., and Tamang, S. (2016). Synthesis of semiconductor nanocrystals, focusing on nontoxic and earth-abundant materials. Chem. Rev. *116*, 10731–10819.

Ren, F., del Rosal, B., An, S.Y., Yang, F., Carrasco, E., Benayas, A., Oh, J.K., Jaque, D., de la Fuente, Á.J., and Vetrone, F. (2017). Development and investigation of ultrastable pbs/cds/zns quantum dots for near-infrared tumor imaging. Part Part Syst. Charact *34*, 1600242.

Resch-Genger, U., Grabolle, M., Cavaliere-Jaricot, S., Nitschke, R., and Nann, T. (2008). Quantum dots versus organic dyes as fluorescent labels. Nat. Methods *5*, 763.

Saikia, D., Chakravarty, S., Sarma, N., Bhattacharjee, S., Datta, P., and Adhikary, N. (2017). Aqueous synthesis of highly stable cdte/zns core/shell quantum dots for bioimaging. Luminescence *32*, 401–408.

Samanta, A., Deng, Z., and Liu, Y. (2012). Aqueous synthesis of glutathione-capped cdte/cds/zns and cdte/cdse/zns core/shell/shell nanocrystal heterostructures. Langmuir *28*, 8205–8215.

Sarkar, S., Le, P., Geng, J., Liu, Y., Han, Z., Zahid, M.U., Nall, D., Youn, Y., Selvin, P.R., and Smith, A.M. (2020). Short-wave infrared quantum dots with compact sizes as molecular probes for fluorescence microscopy. J. Am. Chem. Soc. *142*, 3449–3462.

Schaafsma, B.E., Mieog, J.S.D., Hutteman, M., Van der Vorst, J.R., Kuppen, P.J., Löwik, C.W., Frangioni, J.V., Van de Velde, C.J., and Vahrmeijer, A.L. (2011). The clinical use of indocyanine green as a near-infrared fluorescent contrast agent for image-guided oncologic surgery. J. Surg. Oncol. *104*, 323–332.

Sinatra, L., Pan, J., and Bakr, O.M. (2017). Methods of synthesizing monodisperse colloidal quantum dots. Mater. Lett. *12*, 3–7.

Smith, A.M., Mancini, M.C., and Nie, S. (2009). Second window for in vivo imaging. Nat. Nanotechnol. *4*, 710–711.

Sobhanan, J., Jones, P., Kohara, R., Sugino, S., Vacha, M., Subrahmanyam, C., Takano, Y., Lacy, F., and Biju, V. (2020). Toxicity of nanomaterials due to photochemical degradation and the release of heavy metal ions. Nanoscale *12*, 22049–22058.

Soltesz, E.G., Kim, S., Laurence, R.G., DeGrand, A.M., Parungo, C.P., Dor, D.M., Cohn, L.H., Bawendi, M.G., Frangioni, J.V., and Mihaljevic, T. (2005). Intraoperative sentinel lymph node mapping of the lung using near-infrared fluorescent quantum dots. Ann. Thorac. Surg. *79*, 269–277.

Sonawane, G.H., Patil, S.P., and Sonawane, S.H. (2018). Nanocomposites and its applications. In Applications of Nanomaterials (Elsevier), pp. 1–22.

Stasiuk, G.J., Tamang, S., Imbert, D., Gateau, C., Reiss, P., Fries, P., and Mazzanti, M. (2013). Optimizing the relaxivity of gd (iii) complexes appended to inp/zns quantum dots by linker tuning. Dalton Trans. *42*, 8197–8200.

Stasiuk, G.J., Tamang, S., Imbert, D., Poillot, C., Giardiello, M., Tisseyre, C., Barbier, E.L., Fries, P.H., De Waard, M., and Reiss, P. (2011). Cell-permeable In(III) chelate-functionalized inp quantum dots as multimodal imaging agents. ACS Nano *5*, 8193–8201.

Stummer, W., Pichlmeier, U., Meinel, T., Wiestler, O.D., Zanella, F., Reulen, H.-J., and Group, A.-G.S. (2006). Fluorescence-guided surgery with 5-aminolevulinic acid for resection of malignant glioma: a randomised controlled multicentre phase iii trial. Lancet Oncol. *7*, 392–401.

Sun, J., Wang, W., and Yue, Q. (2016). Review on microwave-matter interaction fundamentals and efficient microwave-associated heating strategies. Materials *9*, 231.

Sun, S., Chen, J., Jiang, K., Tang, Z., Wang, Y., Li, Z., Liu, C., Wu, A., and Lin, H. (2019). Ce6-modified carbon dots for multimodal-imaging-guided and single-nir-laser-triggered photothermal/photodynamic synergistic cancer therapy by reduced irradiation power. ACS Appl. Mater. Inter. *11*, 5791–5803.

Sun, Y.-P., Zhou, B., Lin, Y., Wang, W., Fernando, K.S., Pathak, P., Meziani, M.J., Harruff, B.A., Wang, X., and Wang, H. (2006). Quantum-sized carbon dots for bright and colorful photoluminescence. J. Am. Chem. Soc. *128*, 7756–7757.

Sur, V.P., Kominkova, M., Buchtova, Z., Dolezelikova, K., Zitka, O., and Moulick, A. (2019). CdSe QD biosynthesis in yeast using tryptone-enriched media and their conjugation with a peptide hecate for bacterial detection and killing. Nanomaterials *9*, 1463.

Tamang, S., Lincheneau, C., Hermans, Y., Jeong, S., and Reiss, P. (2016). Chemistry of InP nanocrystal syntheses. Chem. Mater. *28*, 2491–2506.

Tang, R., Xue, J., Xu, B., Shen, D., Sudlow, G.P., and Achilefu, S. (2015). Tunable ultrasmall visible-to-extended near-infrared emitting silver sulfide quantum dots for integrin-targeted cancer imaging. ACS Nano *9*, 220–230.

Tian, R., Ma, H., Zhu, S., Lau, J., Ma, R., Liu, Y., Lin, L., Chandra, S., Wang, S., and Zhu, X. (2020). Multiplexed NIR-II probes for lymph node-invaded cancer detection and imaging-guided surgery. Adv. Mater. *32*, 1907365.

van Embden, J., Chesman, A.S., and Jasieniak, J.J. (2015). The heat-up synthesis of colloidal nanocrystals. Chem. Mater. *27*, 2246–2285.

Vardar, D.O., Aydin, S., Hocaoglu, I., Acar, F.H.Y., and Basaran, N. (2018). Effects of silver sulfide

quantum dots coated with 2-mercaptopropionic acid on genotoxic and apoptotic pathways in vitro. Chem. Biol. Interact. *291*, 212–219.

Wang, J., Zhu, Y., He, N., Sun, Y., Grimes, C.A., and Cai, Q. (2020). Tri-doped alkaline earth sulfide nanoparticles as a new class of highly efficient probe with near-IR stimulated fluorescence for in vivo and ultrasensitive bacteria targeted imaging. Sens. Actuators B Chem. *305*, 127427.

Wei, X., Al Muyeed, S.A., Peart, M.R., Sun, W., Tansu, N., and Wierer, J.J., Jr. (2018). Room temperature luminescence of passivated ingan quantum dots formed by quantum-sized-controlled photoelectrochemical etching. Appl. Phys. Lett. *113*, 121106.

Welsher, K., Liu, Z., Sherlock, S.P., Robinson, J.T., Chen, Z., Daranciang, D., and Dai, H. (2009). A route to brightly fluorescent carbon nanotubes for near-infrared imaging in mice. Nat. Nanotechnol. *4*, 773–780.

Xia, C., Meeldijk, J.D., Gerritsen, H.C., and de Mello Donega, C. (2017). Highly luminescent water-dispersible nir-emitting wurtzite CuInS2/ZnS core/shell colloidal quantum dots. Chem. Mater. *29*, 4940–4951.

Yang, F., Skripka, A., Tabatabaei, M.S., Hong, S.H., Ren, F., Benayas, A., Oh, J.K., Martel, S., Liu, X., and Vetrone, F. (2019). Multifunctional self-assembled supernanoparticles for deep-tissue bimodal imaging and amplified dual-mode heating treatment. ACS Nano *13*, 408–420.

Yang, P., Murase, N., Suzuki, M., Hosokawa, C., Kawasaki, K., Kato, T., and Taguchi, T. (2010). Bright, non-blinking, and less-cytotoxic SiO2 beads with multiple CdSe/ZnS nanocrystals. Chem. Commun. *46*, 4595–4597.

Yu, G.-T., Luo, M.-Y., Li, H., Chen, S., Huang, B., Sun, Z.-J., Cui, R., and Zhang, M. (2019). Molecular targeting nanoprobes with non-overlap emission in the second near-infrared window for in vivo two-color colocalization of immune cells. ACS Nano *13*, 12830–12839.

Yu, M., Zhao, K., Zhu, X., Tang, S., Nie, Z., Huang, Y., Zhao, P., and Yao, S. (2017). Development of near-infrared ratiometric fluorescent probe based on cationic conjugated polymer and CdTe/CdS QDs for label-free determination of glucose in human body fluids. Biosens. Bioelectron. *95*, 41–47.

Yuan, Y., Zhang, Z., Hou, W., Qin, W., Meng, Z., and Wu, C. (2020). In vivo dynamic cell tracking with long-wavelength excitable and near-infrared fluorescent polymer dots. Biomaterials, 120139.

Zhang, H., Salo, D.C., Kim, D.M., Komarov, S., Tai, Y.-C., and Berezin, M.Y. (2016). Penetration depth of photons in biological tissues from hyperspectral imaging in shortwave infrared in transmission and reflection geometries. J. Biomed. Opt. *21*, 126006.

Zhang, A., Pan, S., Zhang, Y., Chang, J., Cheng, J., Huang, Z., Li, T., Zhang, C., de la Fuentea, J.M., and Zhang, Q. (2019a). Carbon-gold hybrid nanoprobes for real-time imaging, photothermal/photodynamic and nanozyme oxidative therapy. Theranostics *9*, 3443.

Zhang, J.J., Lin, Y., Zhou, H., He, H., Ma, J.J., Luo, M.Y., Zhang, Z.L., and Pang, D.W. (2019b). Cell membrane-camouflaged NIR II fluorescent Ag2Te quantum dots-based nanobioprobes for enhanced in vivo homotypic tumor imaging. Adv. Healthc. Mater. *8*, 1900341.

Zhang, M., Yue, J., Cui, R., Ma, Z., Wan, H., Wang, F., Zhu, S., Zhou, Y., Kuang, Y., and Zhong, Y. (2018). Bright quantum dots emitting at~ 1,600 nm in the nir-iib window for deep tissue fluorescence imaging. Proc. Natl. Acad. Sci. U S A *115*, 6590–6595.

Zhang, Y., Hong, G., Zhang, Y., Chen, G., Li, F., Dai, H., and Wang, Q. (2012). Ag2S quantum dot: a bright and biocompatible fluorescent nanoprobe in the second near-infrared window. ACS Nano *6*, 3695–3702.

Zhang, Y., Liu, Y., Li, C., Chen, X., and Wang, Q. (2014). Controlled synthesis of Ag2S quantum dots and experimental determination of the exciton bohr radius. J. Phys. Chem. C *118*, 4918–4923.

Zhang, Y., Yang, H., An, X., Wang, Z., Yang, X., Yu, M., Zhang, R., Sun, Z., and Wang, Q. (2020). Controlled synthesis of Ag2Te@Ag2S core–shell quantum dots with enhanced and tunable fluorescence in the second near-infrared window. Small *16*, 2001003.

Zhao, D., He, Z., Chan, W., and Choi, M.M. (2009). Synthesis and characterization of high-quality water-soluble near-infrared-emitting cdte/cds quantum dots capped by n-acetyl-l-cysteine via hydrothermal method. J. Phys. Chem. C *113*, 1293–1300.

Zhao, F., Xiao, H., Bai, X., and Zu, X. (2019). Effects of ag doping on the electronic and optical properties of cdse quantum dots. Phys. Chem. Chem. Phys. *21*, 16108–16119.

Zhao, P., Xu, Q., Tao, J., Jin, Z., Pan, Y., Yu, C., and Yu, Z. (2018). Near infrared quantum dots in biomedical applications: current status and future perspective. Wiley Interdiscip. Rev. Nanomed. Nanobiotechnol. *10*, e1483.

Zhao, Y., Song, M., Yang, X., Yang, J., Du, C., Wang, G., Yi, J., Shan, G., Li, D., and Liu, L. (2020). Amorphous $Ag_{2-x}Cu_xS$ quantum dots:"All-in-one" theranostic nanomedicines for near-infrared fluorescence/photoacoustics dual-modal-imaging-guided photothermal therapy. Chem. Eng. J. 125777.